

DETECTING GA AIRCRAFT HAZARDOUS STATE USING A LOW-COST ATTITUDE AND HEADING REFERENCE SYSTEM

by

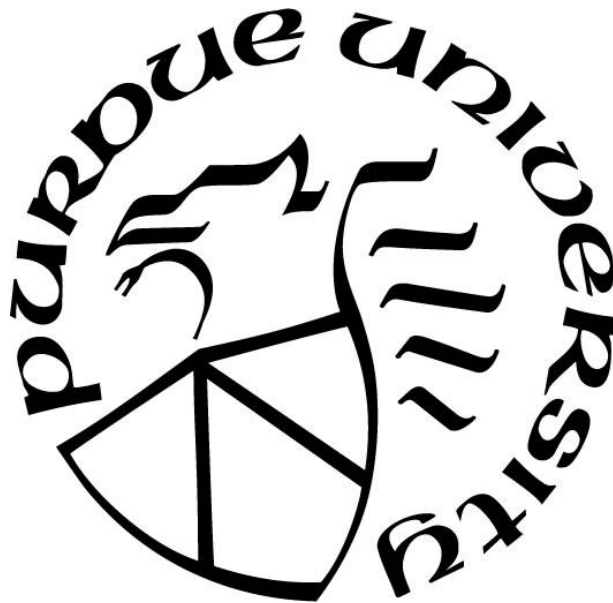
Arpan Chakraborty

A Thesis

Submitted to the Faculty of Purdue University

In Partial Fulfillment of the Requirements for the degree of

Master of Science in Aeronautics and Astronautics



School of Aeronautics & Astronautics

West Lafayette, Indiana

December 2018

**THE PURDUE UNIVERSITY GRADUATE SCHOOL
STATEMENT OF COMMITTEE APPROVAL**

Dr. Karen Marais, Chair

Department of Aeronautics and Astronautics

Dr. William A. Crossley

Department of Aeronautics and Astronautics

Dr. Bruno Ribeiro

Department of Computer Science

Approved by:

Dr. Weinong W. Chen

Head of the Graduate Program

To Mamai and Papai

ACKNOWLEDGMENTS

First, I would like to thank my advisor, Dr. Marais, for her guidance and encouragement. Her advice and insight were invaluable to our research. She helps her students improve holistically, personally and professionally.

Fellow graduate students George, Divya and Nicoletta. Graduate life would not be the same without them. They have helped me through everything; research questions, data collection, document reviews, my weakness for all edibles and in storming a castle with their army. Thank you.

Enrique Babio for helping me understand different aspects of an Attitude and Heading Reference System. Ivan and Natalia Ostroumov for providing guidance on types of results pertaining to this research.

I would like to thank the Federal Aviation Administration (FAA). The US Department of Transportation/Federal Aviation Administration PEGASAS Center of Excellence partially funded this research under Award No 12-C-GA-PU AM44, 55. The project was managed by Michael Vu. The views expressed in this thesis are mine and do not necessarily reflect those of the FAA. The information in this research does not constitute FAA Flight Standards or FAA Aircraft Certification policy.

My friends whom I met in West Lafayette. They made life joyful and exciting in this quaint town.

Finally, I would like to thank my parents. Their support and belief in me motivates me. They are the bedrock of my life.

TABLE OF CONTENTS

LIST OF TABLES	8
LIST OF FIGURES	10
LIST OF ABBREVIATIONS	12
ABSTRACT	13
1. INTRODUCTION	15
1.1 Flight Data in General Aviation.....	16
1.2 Data in the Safety Analysis of General Aviation.....	18
1.3 Research Goals and Thesis Objectives	19
2. ATTITUDE HEADING AND REFERENCE SYSTEM (AHRS).....	21
2.1 AHRS Anatomy	21
2.1.1 Attitude, Attitude Estimation, and Sensor Fusion Algorithm.....	23
2.1.1.1 Attitude or Orientation.....	23
2.1.1.2 Attitude Estimation and Sensor Fusion Algorithm.....	27
2.1.2 Sensor Calibration	28
2.2 Garmin G1000 and GRS 77	29
2.3 Survey of Low-cost IMU and AHRS.....	30
2.3.1 MEMS Sensor Landscape.....	31
2.3.2 Hobbyist Unmanned Aerial Vehicle (UAV) Market.....	32
2.3.3 Survey of Open Source AHRS Software.....	33
2.4 Stratux: Open Source AHRS for GA	34
3. DETECTING HAZARDOUS STATES USING THE STRATUX	37
3.1 Experimental Setup and Data Collection.....	38
3.2 Stratux Data Processing	40
3.2.1 Segregating Flights	41
3.2.2 Syncing G1000 and Stratux data	41
3.3 Characteristics of the Roll Angle Data from the Stratux and the G1000.....	42
3.3.1 Error Definition	42
3.4 Comparison of the Stratux roll data and the G1000 roll data	44
3.4.1 Standard DO-334.....	45

3.4.2	Power Analysis	45
3.4.3	Cross-Correlation and Time Shift between the Stratux and the G1000	46
3.5	Roll Angle Error Characteristics.....	47
3.6	Detecting Hazardous Bank Angle.....	50
3.6.1	Improve Stratux roll angles	51
3.6.1.1	Model 1: Continuous Linear Model	51
3.6.1.2	Model 2: Error Model for Stratux Roll Angles using piecewise Fourier Transfer.....	52
3.6.1.3	Model 3: G1000 Roll Angle Model for Stratux Roll Angles using piecewise Polynomial functions	53
3.6.1.4	Results on Training Set.....	54
3.6.2	Changing Roll Angle Safety Limit for Stratux.....	55
3.6.3	Probability of Detecting Hazardous State ($\phi > 45^\circ$).....	58
3.6.3.1	Probability of our Stratux detecting a G1000 Hazardous State.....	58
3.6.3.2	Probability of Hazardous State occurring at Stratux Angles	59
4.	DETECTING ACCURACY FOR TIME ALONG WITH ANGLE	61
4.1	Definition of Risk Level (RL).....	61
4.2	Definition of Risk Category (RC).....	62
4.3	Risk Level Functions	63
4.3.1	Integration of Angle over Time	64
4.3.2	Two Risk Level Mapping functions	66
4.4	Comparison of Risk Categories between the Stratux and the G1000.....	68
5.	RESULTS: USING THE MODELLED STRATUX AND SOFT LIMITS TO IMPROVE DETECTIONS.....	71
5.1	Detection of Roll Angles above a Defined Hazardous Limit	71
5.2	Detection of Risk Categories when using Soft Limits.....	76
6.	CONCLUSION AND FUTURE WORK	79
	APPENDIX A: LIST OF IMU BREAK-OUT BOARDS AND IMU SENSORS AVAIABLE AS OF SEPTEBER 2017	81
	APPENDIX B. LIST OF STRATUX VARIABLES RECORDED	89

APPENDIX C: THE CONDITIONAL PROBABILITY TABLES OF THE STRATUX RISK CATEGORIES WHEN USING EQUATION(13 TO GENERATE THE RISK LEVELS	95
REFERENCES	96

LIST OF TABLES

Table 1: Differences between the Stratux data collection and the G1000 data collection	40
Table 2: Mean and Variance of Errors for positive and negative roll angles	43
Table 3: Required number data points from power analysis compared to the number of data points we collected for two intervals of roll angles	46
Table 4: Co-efficient values of the linear fit for the error.....	48
Table 5: 95% CI of the slope of the linear fits and the r^2 values, for the two angle intervals shown in Figure 15	49
Table 6: Comparison of Missed Detections (MD) and False Alarms (FA) between the actual Stratux roll angle data and three models to improve the Stratux roll angles on training data set. 55	
Table 7: Scaling Integration Results (IR) to risk level and risk category definitions.....	65
Table 8: Logic of incrementing time and risk level at data points.....	67
Table 9: Conditional Probabilities of the Stratux RC matching the G1000 RC for RL derived from equation 12.....	69
Table 10: Conditional Probabilities of the Stratux RC matching the G1000 RC for RL derived from equation 13.....	70
Table 11: Conditional Probabilities of the Stratux RC matching the G1000 RC for RL derived from equation 14.....	70
Table 12: Comparison of missed detections (MD), false alarms (FA) and correct detections (CD) for the actual and improved Stratux, and for the hard and soft limits for the Stratux when the hazardous angle limit is 45°	71
Table 13: Probabilities of Detection of $ \phi > 19^\circ$	72
Table 14: Probabilities of Detection of $ \phi > 37^\circ$	73
Table 15: Conditional Probabilities of the Stratux RC matching the G1000 RC for RL derived from equation 12 for a hard limit of $ 19^\circ $ on the test data.	76
Table 16: Conditional Probabilities of the Stratux RC matching the G1000 RC for RL derived from equation 12 for the inner soft limit of $ 18.18^\circ $ on the test data.....	77
Table 17: Conditional Probabilities of the Stratux RC matching the G1000 RC for RL derived from equation 12 for the outer soft limit of $ 19.83^\circ $ on the test data.....	77

Table 18: Sum of the diagonal elements, the elements below the diagonal and the elements above the diagonal for Table 15, Table 16 and Table 17	78
Table 19: Sum of the diagonal elements, the elements below the diagonal and the elements above the diagonal of conditional probability tables when we use equation (13.....	78
Table 20: List of Hobbyist IMU breakout boards with 6 or more Degrees of Freedom (DOF)...	81
Table 21: List of IMU Sensors, the manufacturers, unit price and types of sensors, arranged in increasing order of unit price.	83
Table 22: Description of ‘GPSFixQuality’ values.....	91
Table 23: Horizontal positional accuracy corresponding to ‘GPSNACp’ values.....	92
Table 24: Description of State Identification Numbers in the Stratux software.....	94
Table 25: Conditional Probabilities of the Stratux RC matching the G1000 RC for RL derived from equation (13 for a hard limit of $ 19^\circ $ on the test data.....	95
Table 26: Conditional Probabilities of the Stratux RC matching the G1000 RC for RL derived from equation (13 for the inner soft limit of $ 18.18^\circ $ on the test data.	95
Table 27: Conditional Probabilities of the Stratux RC matching the G1000 RC for RL derived from equation 12 for the outer soft limit of $ 19.83^\circ $ on the test data.....	95

LIST OF FIGURES

Figure 1: High Level Schematic Diagram of an AHRS	22
Figure 2: The local navigation frame in North-East-Up format compared to the Earth-Centered, Earth-Fixed (ECEF) frame.....	24
Figure 3: Body frame axes for an aircraft.....	25
Figure 4: IMU Breakout Board and Sensor size compared to micro USB.....	31
Figure 5: The Stratux consists of a Raspberry Pi microcontroller, two antennae, a GPS unit, an IMU, and the SD card with the software.	35
Figure 6: A screen shot of a Google Pixel 5 browser page showing the Stratux AHRS information.	36
Figure 7: The User Interface (UI) of the Stratux Logger application on the Google Pixel 5	38
Figure 8: The mount ensures that the location and direction of the equipment is consistent in all flight tests.....	39
Figure 9: Each data structure contained flight variable information.	40
Figure 10: The direction sign associated with the angle is the same in both the G1000 and the Stratux. Right turns are positive and left turns are negative.	42
Figure 11: The roll angle error between the Stratux and the G1000 has large variations.	43
Figure 12: Stratux (Left - a) and G1000 (Right - b) roll data histogram distribution show the large concentration of data in lower magnitude angles	44
Figure 13: Maximum cross-correlations between the G1000 and the Stratux roll angles occurs at Lag = 0.	47
Figure 14: Linear fit for Error vs the G1000 roll angles.....	48
Figure 15: (a) Linear fit of the error for the G1000 roll angle interval of 35° to 45° . (b) Linear fit of the error for the G1000 roll angle interval of -61° to -55°	49
Figure 16: Missed Detections and False Alarms of the Stratux compared to the G1000 for a hazardous roll angle limit of 45°	51
Figure 17: Single Linear Model of the G1000 roll angle from the Stratux roll angles.....	52
Figure 18: Models for the Error from 10° intervals of the Stratux roll angles	53

Figure 19: Models for the G1000 roll angles from 10° intervals of the Stratux roll angles	54
Figure 20: Change of Hard limits to Soft (Red Bands) Limits for the Stratux for an example flight data.....	57
Figure 21: Missed Detections and False Alarms of actual Stratux roll angles compared to the G1000 roll angles when we use soft limits of 45°.....	57
Figure 22: G1000 Roll Angle PDF for the actual Stratux roll = 40° and the area under the curve beyond hard limit of 45° is the probability of HS.....	59
Figure 23: Probability of HS occurring for all Stratux Angles.....	60
Figure 24: Our choices for RC demarcations based on RL	63
Figure 25: Risk Level between t_{start} and t_{end} is the result of integration of the angle over time. ..	64
Figure 26: Comparison of risk level (Left – a) and of risk category (Right – b) from the Stratux and the G1000 when we use the integration of angle over time to find the risk level values	66
Figure 27: Increment time information for computing varying risk level	66
Figure 28: Comparison of risk level (Left – a) and of risk category (Right – b) from the Stratux and the G1000 when we use a predefined mapping function to find the risk level values.....	68
Figure 29: Correct Detection probabilities for varying roll angles for roll data in test flights. Model improved Stratux does not increase correct detections and do not perform well on test data.....	74
Figure 30: Correct Detection probabilities for varying roll angles for roll data in training flights. Modelled Stratux roll angle only marginally improve the detection and is specific to training data.....	75

LIST OF ABBREVIATIONS

<i>GA</i>	=	General Aviation
<i>AHRS</i>	=	Attitude and Heading Reference System
<i>FAA</i>	=	Federal Aviation Administration
<i>FOQA</i>	=	Flight Operational Quality Assurance
<i>FDM</i>	=	Flight Data Management
<i>IMU</i>	=	Inertial Measurement Unit
<i>GNSS</i>	=	Global Navigation Satellite System
<i>GPS</i>	=	Global Positioning System
<i>ADS-B</i>	=	Automatic Dependent Surveillance – Broadcast
<i>HS</i>	=	Hazardous State
<i>MD</i>	=	Missed Detection
<i>FA</i>	=	False Alarms
<i>RMSE</i>	=	Root Mean Square Error
<i>PDF</i>	=	Probability Density Function
<i>CDF</i>	=	Cumulative Density Function
<i>RL</i>	=	Risk Level
<i>RC</i>	=	Risk Category
<i>IR</i>	=	Integration Results.

ABSTRACT

Author: Chakraborty, Arpan. MS

Institution: Purdue University

Degree Received: December 2018

Title: Detecting GA Aircraft Hazardous States Using a Low-Cost Attitude and Heading Reference System.

Major Professor: Dr. Karen Marais

General Aviation (GA) accidents constitute the majority of aviation related accidents. In the United States, there have been over 7,000 GA accidents compared to 190 airline accidents in the last 8 years. Flight data analysis has helped reduce the accident rate in commercial aviation. Similarly, safety analysis based on flight data can help GA be safer. The FAA mandates flight data recorders for multi-engine and turbine powered aircraft, but nearly 80% of General Aviation consists of single engine, of which only a small portion contain any form of data recording device. GA aircraft flight data recorders are costly for operating pilots. Low-cost flight recorders are few and rarely used in GA safety analysis due to lack of accuracy compared to the certified on-board equipment. In this thesis, I investigate the feasibility of using a low-cost Attitude and Heading Reference System (AHRS) to detect hazardous states in GA aircraft. I considered the case of roll angles and found that the low-cost device has significant measurement errors. I developed models to correct the roll angle error as well as methods to improve the detection of hazardous roll angles. I devised a method to evaluate the time accuracy along with the angle accuracy and showed that despite the errors, the low-cost device can provide partial hazardous state detection information.

1. INTRODUCTION

General Aviation (GA) is all civil aviation operations other than scheduled air services and non-scheduled air transport operations for remuneration or hire [ICAO, 2009]. In the FAA's General Aviation Information [FAA, 2008], GA flights are described as flights conducted by operators other than Title 14 of the Code of Federal Regulations (14 CFR) part 121 or part 135 certificate holders. There are over 211,000 GA aircraft in U.S., flying over 24.8 million flight hours to about 5,000 U.S. public airports [GAMA, 2017].

However, GA lags commercial aviation in terms of safety. There have been over 7000 GA accidents compared to 190 airline accidents in the last 8 years. Over the past 10 years, the FAA has taken several initiatives to reduce GA accidents. From 2005 to 2016, the number of total GA accidents and fatal accidents decreased by 57% [FAA, 2018]. However, fatal GA accidents still made up 94% of all fatal accidents in aviation in 2016 [NTSB, 2016]. GA safety, though better than it was in 2005, is still far from the safety levels achieved by commercial aviation. The reduction in fatal accident rates is an indication of steps taken in the right direction, but more steps need to be taken to further decrease the GA accident rate.

Aircraft data is crucial in analyzing and identifying risk. With programs such as the Aviation Safety Information Analysis and Sharing Program (ASIAS) and the 'Got Data? External Data Initiative', the FAA has shown the need for good quality data in GA safety analysis to improve the safety of GA [FAA, 2018].

1.1 Flight Data in General Aviation

Flight Operational Quality Assurance (FOQA), also known as Flight Data Management (FDM), has had a role in commercial aviation since the 1960s. FOQA is a voluntary safety program that is designed to make commercial aviation safer by allowing commercial airlines and pilots to share de-identified aggregated information with the FAA so that the FAA can monitor national trends in aircraft operations and address operational risk issues (e.g., flight operations, air traffic control (ATC), and airports) [AC No: 120-82, 2004]. A Flight Safety Foundation study found that airlines with an active FDM program have accident rates that are 50% lower than carriers without FOQA, and carriers that have used FOQA for the longest also have the fewest accidents [Lau, 2007]. We could potentially decrease the large number of GA accidents by implementing the FOQA philosophy in GA. The General Aviation Joint Steering Committee (GAJSC) has emphasized the need for FOQA and flight data for proactive safety analysis through FAA's Aviation Safety Information Analysis and Sharing (ASIAS) [FAA, 2018].

However, FOQA for GA faces several road blocks:

- FOQA requires in-flight aircraft information recording devices. Commercial aircraft have a variety of sensors and recording devices to enable FOQA. Regulations do not require small, single engine GA aircraft to be equipped with Flight Data Recorders (FDRs). As per 14 CFR 91.609, only multiengine, turbine-powered airplane or rotorcraft having a passenger seating configuration of 10 or more that have been manufactured after October 11, 1991 are required to have a flight data recorder, and only those with a passenger seating configuration of 6 or more are required to have a cockpit voice recorder.

- Many GA aircraft do not have any electronic avionic system. Quick Access Recorders (QAR) help collect raw flight data by directly connecting to the aircraft avionic system. One can use a QAR to collect flight data irrespective of a flight data recorder being on-board or not. Without an electronic avionic system containing digital flight data, in-flight data acquisition is difficult in GA.
- A GA aircraft equipped with an on-board Electronic Flight Instrument System (EFIS) can record aircraft data. EFIS flight data from GA aircraft include GPS data, Attitude, Heading Reference System (AHRS) data, communication/navigation information, and engine information. However, only new GA aircraft contain EFIS, and the cost of retrofitting an old GA aircraft with a new EFIS is over \$10,000. Many of the GA operators are the pilots who either rent or own the aircraft. Unlike airline operators, most of these GA pilots do not have any financial return on investment on the purchase of expensive in-flight data recorders.

Independent Flight Data Recorders (iFDR) and Electronic Flight Bag (EFB) applications can record flight data external to the avionic system on-board. iFDRs and EFBs do not require any certification, but the FAA has provided advisory guidelines for their use [AC No: 91.21-1D, 2017; AC No: 120-76C, 2014]. iFDR, also known as Lightweight Aircraft Recording Systems, are low-cost devices that do not connect to on-board aircraft systems. They collect flight data using their own sensors. For example, iFDRs include video or sound recording devices to record cockpit instruments. EFB applications can record GPS, traffic and weather data, but they require external Attitude Heading and Reference Systems (AHRS) to provide aircraft orientation. Pilots can

connect commercial portable AHRS devices to the handheld device system applications and potentially record data, but these devices cost approximately \$1,000 per system.

1.2 Data in the Safety Analysis of General Aviation

GA safety analyses in the literature primarily use EFIS flight data. Previous safety analyses have used Garmin G1000 EFIS data to identify phases of flight [Goblet et al., 2015], to detect safety events during the approach phase of flight [Fala and Marais, 2016], and to detect anomalies in GA operations [Puranik and Mavris, 2018]; and the Vision 1000 camera to record and create flight tests for a helicopter [Kuo et al., 2017].

Since many GA aircraft do not have an EFIS and many pilots cannot afford expensive on-board equipment, we need low-cost flight data recording options to enable more widespread GA safety analysis. Several researchers have investigated the use of low-cost sensors to collect flight data in GA. Neuhart et al. (2009) acquired flight test data of a Cessna 172S aircraft using low-cost, custom-made hardware and software for simulation validation. The study used over ten types of sensors to monitor pilot inputs, engine performance, control surface deflections, and environmental conditions. The researchers concluded that the flight test data set was of sufficient content and quality to validate a simulation with good fidelity, with a special focus on stability and control characteristics. Valasek et al. (2017) used low-cost Inertial Measurement Units (IMUs) to characterize the derived angle-of-attack (AOA). This study directly used IMU sensor data and not the attitude and heading derived from the IMU (see section 2.1.1). The researchers found that in the case of low sensor noise, the derived AOA tracked the true AOA, but they had insufficient data to draw conclusions in the case of large sensor errors. Albéri et al. (2017) tested the accuracy of low-cost GNSS, radar and barometric sensors for in-flight altitude measurements for airborne radio

metric surveys. The researchers equipped an aircraft with seven altimetric sensors (three low-cost GNSS receivers, one inertial measurement unit, one radar altimeter and two barometers), and found that over the sea, two barometric altimeters together with the radar altimeter performed the most accurate measurement of flight altitude over the sea in the 35–66m range. The study shows how increasing redundancy in low-cost data collection can increase accuracy. Bonadonna et al. (2015) recommended the design requirements for a low-cost flight data recorder to obtain and analyze flight data as described in a pilot operating handbook (POH) of an experimental aircraft. They recommend the use of Garmin Virb to video monitor the flight data and use low-cost microcontrollers such as the Arduino Mega to collect and process the video data.

Researchers so far have used and analyzed low-cost sensors in aircraft data collection. In the examples above, the low-cost data collection led to simulator validation, angle-of-attack derivation and generating a POH for experimental aircraft. The question remains: Can we use the data collected via low-cost sensors for GA safety analysis in the same manner as the data used from an EFIS such as the Garmin G1000?

1.3 Research Goals and Thesis Objectives

In our research, we investigated the feasibility of using roll angle collected from a low-cost AHRS (the Stratux) to detect the hazardous state of high roll angles ($\phi > 45^\circ$) for a GA aircraft compared to the detection when using the data from a Garmin G1000.

We explored the technical knowledge requirements for building a low-cost AHRS and whether one could build a low-cost AHRS using open source software and hobbyist hardware for GA safety analysis (Section 2).

In section 3 we assembled a low cost AHRS (the Stratux) unit and collected flight data for 29 training flights on SR-20 aircraft at Purdue University. We also collected the flight data from the on-board Garmin G1000 on the same aircraft for those 29 flights. We tested the Stratux in detecting high roll angles ($\phi > 45^\circ$) in comparison to the Garmin G1000. We considered the data from the G1000 on-board the SR-20 aircraft to provide the best obtainable measurement of the actual roll angle. The error between the Stratux roll angle and the G1000 roll angle was large and varied with angle. We examined different types of mathematical models that could help to correct the error in the Stratux roll angle measurements. We also varied the definition of the hazardous roll limit (45°) when applied to the Stratux to improve detections of the hazardous state.

Beyond the hazardous roll angle limit of 45° , risk may increase because of higher deviation from the limit or due to longer time spent at hazardous roll angles. We developed a method to evaluate the time accuracy along with the angle accuracy in section 4

We provide the results of our research in section 5 and the potential future work required (Section 6).

2. ATTITUDE HEADING AND REFERENCE SYSTEM (AHRS)

Attitude Heading and Reference Systems (AHRS) are commonly used in commercial and business aircraft. The AHRS information is used in displaying the aircraft attitude on a glass cockpit primary flight display and in the aircraft's autopilot. It provides aircraft attitude through pitch and roll angles. The AHRS also provides the aircraft heading angle. The pitch, roll, and heading angles are important information in determining whether the aircraft is in an unsafe state.

Currently, portable commercial AHRS for general aviation can provide information to handheld devices, such as a tablets or smartphones. The information can be portrayed through a system application in the form of a primary flight display or an electronic attitude indicator. The market price for a portable AHRS ranges from \$800 to \$1,500. These portable AHRS are often found in combination with ADS-B In receivers. The high cost of the commercial portable AHRS is due to multiple complexities of an AHRS device and the accuracy level required, as discussed in this chapter.

2.1 AHRS Anatomy

An inertial measurement unit (IMU) consists of an accelerometer and a gyroscope. A Magnetic, Angular Rate and Gravity (MARG) is an IMU with a magnetometer. An AHRS device is an IMU or a MARG and a processing unit containing the attitude estimation logic. In academic research the difference between IMUs, MARGs and AHRSs is well established, but in the consumer market IMUs and MARGs are treated as the same and referred to as IMUs. The primary difference between an AHRS and an IMU is that an IMU only provides sensor data. It does not contain

estimation algorithms for computing attitude or heading. Figure 1 shows a structural composition of an AHRS unit used in aviation.

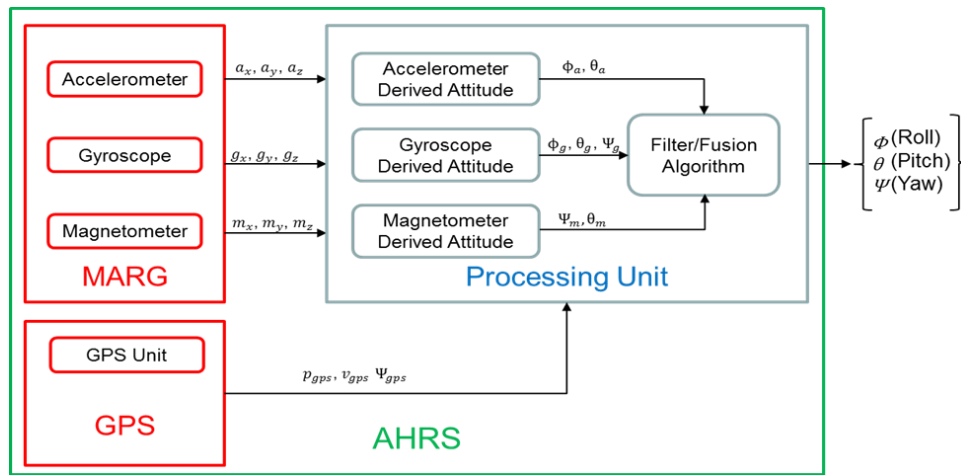


Figure 1: High Level Schematic Diagram of an AHRS

Sensors are of various types and grade. Sensor type defines the fundamental methodology used in sensing. Use of optical fibers in fiber optic gyros (FOGs), laser in accelerometers, and micro electromechanical systems (MEMS) are a few examples. The grade of the sensor depends on the accuracy and level of noise in the sensor output. The grade can be improved by calibrating the sensor output for known or estimated noise. Low-cost sensors are often also called automotive grade sensors or consumer grade sensors. Sensors used in aviation are higher in accuracy and reliability than automotive grade sensors and are referred to as industrial grade sensors.

Some low-cost commercial IMUs available in the market are also rudimentary AHRS devices since they contain a microcontroller and basic level of estimation logic for obtaining attitude information. The attitude information is noisy and provides highly erroneous values over time when the body accelerates with respect to an inertial frame.

2.1.1 Attitude, Attitude Estimation, and Sensor Fusion Algorithm

In this section we review the definition of aircraft attitude and explore the algorithms that are used to estimate aircraft attitude from sensor data.

2.1.1.1 Attitude or Orientation

Attitude is described between two frames. One is an inertial frame which is fixed in time and is not rotating or accelerating. The second frame is the object or body frame for which we measure the orientation. The two coordinate frames have orthogonal right-handed axes, and the position and orientation of each frame can be described with respect to one another.

In aircraft attitude estimation the local navigation frame (also known as the local geodetic or tangent plane) is the inertial frame. In aviation, the local navigation frame, shown in Figure 2, is in the North-East-Down format. It is described by the z-axis pointing towards the direction of gravity and the x-axis orthogonal to the z-axis pointing towards the magnetic North Pole. By the right-hand rule, the y-axis becomes the axis pointing to the east and orthogonal to both x and z-axes.

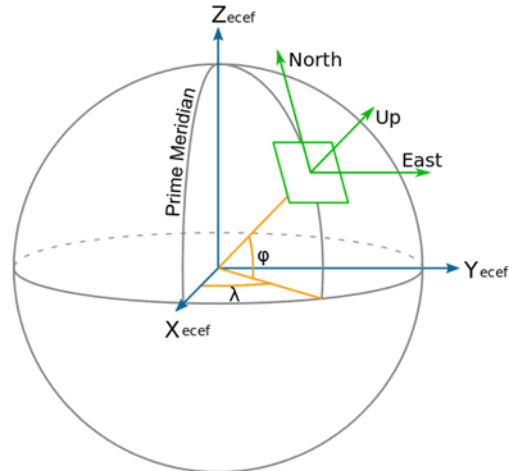


Figure 2: The local navigation frame in North-East-Up format compared to the Earth-Centered, Earth-Fixed (ECEF) frame.

The body frame (denoted by superscript **b** in Figure 3) has the same origin as that of the local navigation frame and it lies within the body for which we intend to find the attitude. The axes are fixed with respect to the body. In the case of an aircraft, the origin is the center of gravity. The x-axis is the axis pointing from the center of gravity to the nose of the aircraft. It is the roll axis of the aircraft. The y-axis points from the center of gravity to the right wingtip and is the pitch axis of the aircraft. The z-axis, by the right-hand rule, is downwards and orthogonal to the other two axes and is the yaw axis of the aircraft.

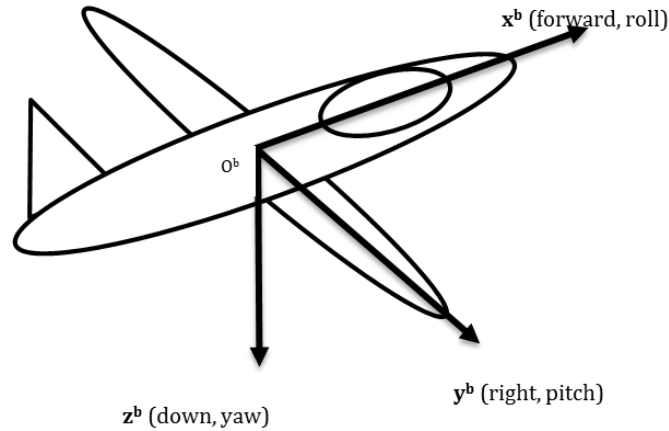


Figure 3: Body frame axes for an aircraft.

The attitude of the body frame is the degree of angular rotation of the body frame with respect to the inertial local navigation frame. There are several methods to describe attitude. The three commonly used methods are:

- Euler Angles: Euler Angles are the consecutive rotations of the body frame about inertial frame axes starting with both frames coinciding to finally reach the body frame attitude. There are two intermediate frames between the initial and final state of the body frame. The first rotation is about the common z-axis and is the ‘yaw’. The second rotation is the ‘pitch’ rotation about the common y-axis is the first intermediate frame. Finally, the ‘roll’ rotation about the common x-axis is the second intermediate frame. The vector containing the 3 angles is called the set of Euler Angles. It is intuitive and easy to visualize attitude using the Euler angle representation. The final output of an AHRS is in Euler angle representation. However, the Euler angle representation poses mathematical problems in computation. At $+90^\circ$ pitch, the yaw and roll angle become indistinguishable. This phenomenon is known as a ‘gimbal lock’ [Paul D. Groves, 2008].

- **Coordinate Transformation Matrix:** The coordinate transformation matrix, or the rotation matrix, is a 3x3 orthogonal matrix ($C_{i \rightarrow b}$) that transforms a vector in the inertial frame (x_i) to a vector in the body frame (x_b).

$$x_b = C_{i \rightarrow b} * x_i \quad (1)$$

One can show the coordinate transformation as a matrix of cosines of angles between the unit vectors of the frames, due to which these matrices are also called Direct Cosine Matrices (DCM). The coordinate transformation matrix representation of attitude can be manipulated easily. We can achieve several rotations by simply multiplying the matrices of each rotation. To find the original vector we need to use the inverse of the matrix. However, the coordinate transformation matrix is computationally intensive [Paul D. Groves, 2008].

- **Quaternions:** Quaternions are hypercomplex representations of attitude. An attitude represented by Quaternions consists of a vector containing four elements: $q = (q_0, q_1, q_2, q_3)$, where q_0 is the scalar component of the Quaternion and represents the magnitude of the rotation. The remaining three elements of the vector are complex components of the quaternion and represent the axis about which the rotation takes place. Quaternion algebra is complicated but has low computational requirements. The mathematical problem of ‘gimbal lock’ is avoided during attitude computation using the Quaternion representation.

The three methods of attitude representation are interchangeable in form. Due to this flexibility, the majority of the AHRS attitude estimation logic performs the computation in Quaternion form and outputs the result in either Euler angles or Coordinate transformation matrix form.

2.1.1.2 Attitude Estimation and Sensor Fusion Algorithm

Attitude estimation and sensor fusion is a large research field on its own. We can estimate attitude from angular rate and from vector observations [Madgwick, 2010]. We can also compute attitude at a time t by numerical integration of the angular rate from the gyroscope with time, provided we know the initial attitude.

The accelerometer and magnetometer measure the magnitude and direction of the reference frame with respect to the body frame. “Single-frame” algorithms estimate attitude based on measurements taken at a single time [Markley and Mortari, 2000]. The first person to propose the problem relating to single frame attitude estimation was Grace Wahba in 1965 [Wahba, 1965]. Wahba’s problem was to find the optimal 3x3 rotational matrix to minimize the cost function: $L(M)$ for $n \geq 2$. In equation 2, x_i and x_b denote the unit vectors in the inertial reference frame and the body frame respectively. a_i are the weights used for the weighted optimization:

$$L(M) = \frac{1}{2} * \sum_{i=1}^n a_i * (x_i - Mx_b)^2 \quad (2)$$

Several solutions exist in the literature to the Wahba Problem. The popular solutions are the Three-Axis-Attitude-Determination (TRIAD), Quaternion Estimator (QUEST), Davenport’s q-method, Fast Optimal Matrix Algorithm (FOAM), Single Value Decomposition (SVD) and Polar Decomposition (PD) [Valenti et al., 2015].

Errors in attitude estimation may be due to several factors. Sensor noise errors arise based on the type and grade of the sensors and calibration performed compared to the level of accuracy required. Errors may also be due to external factors such as a strong local magnetic field impacting the

output of a magnetometer. Numerical integration of gyroscope angular rate also integrates the gyroscopic errors and propagates them with time.

If the body frame accelerates or performs dynamic turns with respect to the inertial reference frame, then the accelerometer measures the body frame accelerations and the acceleration due to gravity. From the accelerometer measurements, the acceleration due to gravity and the body acceleration are indistinguishable and the orientation vectors in the direction of gravity are skewed. In such cases, body frame position and velocity estimation are required to estimate body frame acceleration and thereby find accurate gravity vectors to be used in attitude estimation. In many aerospace applications a GPS is used in combination with the given sensors to correct vector measurements.

To negate the impact due to large possibilities of errors and obtain accurate attitude, the attitude estimations from angular rate, vector measurements, and GPS data are fused together. The choice of fusion algorithm used is based on accuracy of estimation achievable, the processing capabilities, and the execution time. Primarily, the industry uses Kalman Filters and the Extended Kalman Filters as fusion algorithms [XSENS, 2018] [Vectornav, 2018] [Madgwick, 2010]. The literature provides several alternatives and improvements to the Kalman Filter as a sensor fusion algorithm [Valenti et al., 2015].

2.1.2 Sensor Calibration

Different user levels define calibration differently. In general, calibration means “sensor calibration”. At a system user level, calibration defines the final setup for use. In this case, the

AHRS calibration is defined as the orientation of placement within the aircraft to determine the initial orientation and thereby correct future responses.

Low-cost sensors produce a lot of noise. Sensors from the same manufacturer may provide different results for the same input. All sensors require three primary calibrations:

- **Sensor Bias:** The output for zero input. Gyroscope bias varies with time and is called the gyroscopic random drift/walk.
- **Scale Factor:** The sensor output response to a known input.
- **Axis misalignment:** Interdependency of sensor axis readings.

Different operational temperature and vibration ranges require all the above calibrations. The magnetometer requires two additional calibrations:

- **Hard Iron:** Known fixed magnetic field influencing sensor output.
- **Soft Iron:** Varying magnetic field influencing the sensor output.

These calibrations require expensive equipment and extensive technical knowledge. Many commercial companies use low-cost sensors for AHRS but spend thousands of dollars in calibrating every MEMS sensor they use. The calibration is one of the main drivers of the high cost of commercial AHRS units.

2.2 Garmin G1000 and GRS 77

A popular EFIS is the Garmin G1000 Integrated Avionics system used in several General Aviation aircraft. Integrated avionics consists of multiple Line Replaceable Units (LRUs). The GRS77 is the Attitude and Heading Reference System LRU within the G1000 [Garmin, 2015]. GMU44 is an external magnetometer LRU which senses and provides local magnetic field information to

support the function of the GRS77 [Garmin, 2010]. Garmin uses the SAE AS 8001 as the minimum performance standard for bank (roll) and pitch instruments [Garmin, 2010].

The GRS77 installation manual provides the operational limits and accuracy: *The GRS 77/GMU 44 is capable of maneuvers through a range of 360° in bank (roll) and pitch. The rotation rate capability is ±200° per second. However, ARINC 429 angular rate output messages are limited to ±128° per second. Bank (roll) error and pitch error are within ±1.25° over the range of 30° bank(roll), left and right, and 15° pitch nose up and nose down. Heading is accurate to within 2° in straight and level flight* [Garmin, 2010].

2.3 Survey of Low-cost IMU and AHRS

Microelectromechanical systems (MEMS) are a technology used to create tiny integrated devices or systems that combine electrical and mechanical components [PRIME Faraday Partnership, 2002]. MEMS are fabricated using integrated circuit (IC) batch processing techniques and can range in size from a few micrometers to millimeters. MEMS devices (or systems) can sense, control, and actuate on the micro scale, and generate effects on the macro scale.

MEMS have many applications in the automotive, electrical, medical, and defense industries. Advancement in MEMS technology has reduced the size, weight, power consumption, and cost of the sensors used in IMUs. Sensor sizes range from 0.001mm to 0.1mm [PRIME Faraday Partnership, 2002; Dejan, 2018].

In comparison to more expensive Fiber Optic IMU sensors, MEMS IMU sensors have degraded performance [KVH Industries, 2014]. However, due to their low cost, size and weight, MEMS

IMUs have become very popular in the consumer market. Nearly all smartphones, hobby drones and UAVs, and pedometers use low-cost MEMS IMU sensors.

2.3.1 MEMS Sensor Landscape

An AHRS unit requires an IMU with at least a 3-axis accelerometer, 3-axis gyroscope. An IMU containing a 3-axis accelerometer, 3-axis gyroscope is termed as an IMU with 6 degrees-of-freedom (DOF). Addition of a 3-axis magnetometer increases the DOF to nine. In the consumer market, the maximum DOF of an IMU is 10. A 10 DOF IMU contains a 3-axis accelerometer, 3-axis gyroscope, 3-axis magnetometer, and a barometer that senses temperature and pressure. We explored the available low-cost IMUs with six or more degrees of freedom in the consumer market.

The major smart phones (e.g., iPhone, Samsung S8) all use similar grade MEMS sensors. All the MEMS IMU devices cost less than \$5 and are created by a small number of manufacturers. Hobbyist and Do-It-Yourself (DIY) electronic companies, such as SparkFun and Adafruit, make MEMS sensors available to the common consumer by putting MEMS sensors onto surface mounted technology (SMT) boards called ‘evaluation’ sensor boards or breakout boards. Figure 4 shows the size comparison of a breakout board and a USB cable.



Figure 4: IMU Breakout Board and Sensor size compared to micro USB

Some of the breakout boards contain a microcontroller. If there isn't a microcontroller, one can be soldered on through the appropriate breakout points. The breakout boards containing MEMS IMUs cost about \$50. APPENDIX A lists the Sensors and IMU boards available in the market as of September 2017. Robotics hobbyists typically use the breakout board because it provides breakout pins to connect additional sensors or a microcontroller to the IMUs. The microcontrollers on breakout boards can often be coded using an Integrated Development Environment (IDE). Example code and firmware for breakout boards are available in open source for hobbyists to retrieve sensor data and use the IMU. However, each manufacturer has their own IDE, which is an additional effort for the end user while evaluating different IMU boards with different microcontrollers.

DIY electronic equipment manufacturers market their products based on the degrees-of-freedom of the IMU, the complexity of motion sensing algorithms available in open source, the accuracy and range of sensors, and the available communication mechanisms on board. Universal Asynchronous Receiver/Transmitter (UART), Serial Peripheral Interface (SPI) and Inter-Integrated Circuit (I2C) are the commonly available Interfaces with I2C being the newest technology and the most popular. I2C data communication consists of 2 buses (SDA and SLA), and a user can connect several 'master' and 'slave' devices to the same bus. Therefore, a user can attach more than one processing unit to the same IMU.

2.3.2 Hobbyist Unmanned Aerial Vehicle (UAV) Market

Autopilots and Flight controllers are popular in the UAV world. There are many high quality, reasonably priced options. Open source forums such as Ardupilot provide material, guidelines, instruction, and resources in building a UAV. The autopilots commonly used in UAV fixed wings

are Pixhawk and Navio+. They both contain multiple IMUs and produce AHRS data for control of the aircraft. However, since these systems are primarily focused on the UAV market, decoupling AHRS data from UAV autopilot system for a GA aircraft has the following disadvantages:

- Higher cost than conventional IMUs and microcontrollers due to additional capabilities.
- Requires additional installation of Ground control systems, which vary depending upon requirements in the UAS world.
- Pixhawk systems work once the autopilot is connected to a remote control. Leads to higher equipment cost which are truly not necessary for AHRS information in GA. Navio+ do provide AHRS code, but no documentation exists on accessibility of just the AHRS data.

2.3.3 Survey of Open Source AHRS Software

The most popular open source, orientation and sensor filter algorithms are Mahony and Madwig filters [Townsend, 2018; X-IO Technologies, 2018]. Implementations of these algorithms are available in MATLAB, C and C#. The Madwig and Mahony filters provide good orientation estimation with low computational time and are popular for small-scale UAV and robotic applications [Madgwick, 2010; Mahony et al., 2008]. However, these filters do not consider non-inertial acceleration and cannot be used in applications where large centripetal accelerations are experienced in the body frame. To determine non-inertial acceleration, an external GPS unit or Pitot-static system information is required [Mahony et al., 2011].

Orientation algorithms consisting of Kalman filter (KF) and Extended Kalman filter (EKF) as sensor fusion algorithms are available in the open literature and implementations are available on open source platforms. However, the open source implementations have the following drawbacks:

- An implementation exists but the applicable hardware is unknown. The interface linking hardware to the estimation algorithm is not present or is unique to a certain type of hardware.
- They are not well maintained, as there is no link to a commercial entity. KF and EKF require processing power greater than what is commonly available to a robotics enthusiast.

2.4 Stratux: Open Source AHRS for GA

We acquired a low-cost device which currently has users from the GA community and is easy to build. Stratux is a low-cost ADS-B In receiver and AHRS that pilots can build on their own. The hardware for building the Stratux is inexpensive and can be acquired from various suppliers on hobby websites or popular e-retailers. The Stratux software is open source. [Stratux, 2018]. We are interested in the AHRS data from the Stratux in this research. The net cost of our Stratux was \$146. Figure 5 shows the assembled hardware components of the Stratux and their relative sizes to a ruler and a quarter. The Stratux does not have an internal power unit and requires an external battery. We used a MI 10400mAh power bank to power the Stratux during flight tests.

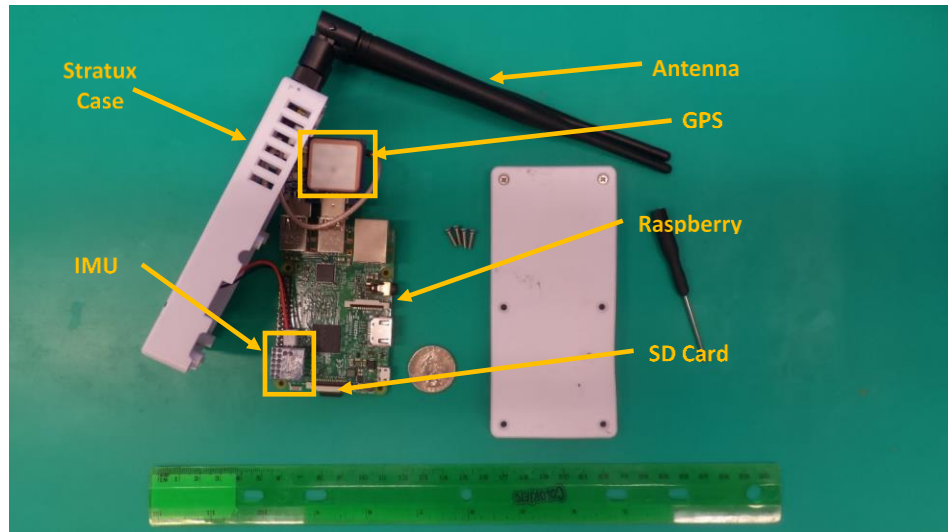


Figure 5: The Stratux consists of a Raspberry Pi microcontroller, two antennae, a GPS unit, an IMU, and the SD card with the software.

A user can download the Stratux software on an 8GB (or greater) SD card, plug the SD card into the Raspberry Pi, power the Stratux and use the device. The Stratux software is written in ‘Go’ language. ‘Go’ is an open source programming language created by Google. For our research we used stratux-v1.4r5 and stratux-v1.4r4 versions of the Stratux software. The Stratux software through the Raspberry Pi creates a Wi-Fi network. A user can connect handheld devices to this Wi-Fi. Similar to the commercially available portable ADS-B and AHRS devices, a user can access Stratux data through majority of the popular Electronic-Flight-Bag (EFB) applications and also visualize Stratux data without any application by accessing the Stratux webpage (<http://192.168.10.1>). Figure 6 shows a screenshot of the AHRS information displayed on a browser on a smart phone.

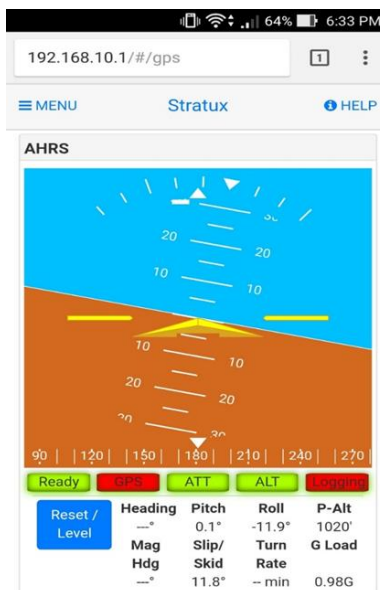


Figure 6: A screen shot of a Google Pixel 5 browser page showing the Stratux AHRS information.

Even though the Stratux has an SD card onboard, it does not record any flight data. It only records system debug information. Stratux provides flight data over the Wi-Fi network using the GDL90 protocol over port 4000. It also provides certain specific data sets over webservers [Stratux App Integration, 2018]. The webserver <http://192.168.10.1/getSituation> provides the GPS and AHRS information. To record the Stratux flight data a user would have to use an existing EFB application or build an application and use the existing infrastructure to record and store the data.

3. DETECTING HAZARDOUS STATES USING THE STRATUX

States are segments of time wherein a system exhibits a particular behavior. A hazardous state is a system state that may lead to an accident or an incident if corrective action is not taken and the system remains in the hazardous state for extended time [Rao and Marais, 2016]. A high roll angle (ϕ) is an example of such a hazardous state. For example, on January 25th, 2017 a Cirrus SR-22 airplane crashed while on the right turn to the final approach leg to runway 32 at the Stinson Municipal Airport in San Antonio, Texas. The aircraft was approaching the runway at a calibrated speed of 103 knots, at 200 feet above the ground and in an approximate roll angle of 48° and entered a descent which exceeded 1,800 fpm. The report concluded that the aircraft crashed due to the aircraft stalling at high roll angle and excessive side slip [NTSB, 2018]. Corporate flight operational quality assurance (C-FOQA) of unstable approaches from 2009 also identified high roll angle for given height as the third most frequent cause for unstable approaches [Darby, 2010].

The definition of hazardous roll angle depends on operation, pilot certification, and phase of flight. We propose future work to determine hazardous roll angles from GA ASIAs in section 5.5. The Stratux provides the aircraft roll and pitch information. The analysis here is based on detecting angles beyond a user-defined hazardous roll angle limit, beyond which we consider the flight to be risky.

For the scope of this research we assumed the Garmin G1000 AHRS as the ‘gold standard’. The Garmin G1000 has errors (see section 2.2), but the errors are within the FAA’s minimum performance standards. There was no method via which we could find the exact errors of the Garmin G1000 from which we received the data. Due to the lack of a higher accuracy system

available in the GA aircraft we flight tested and the prevalent use of Garmin G1000 for safety analysis in GA, we used the Garmin G1000 AHRS values as the truth.

3.1 Experimental Setup and Data Collection

Even though the Stratux provides roll and pitch data, there is no recording capability. We developed an Android application, the Stratux Logger, to collect GPS and AHRS information from the Stratux webserver. APPENDIX B provides the list of the variables and their descriptions. Figure 7 shows the screenshot of the Android application on a Google Pixel 5 phone. The G1000 records data every 1 second and the Stratux Logger application collects data every 900 millisecond. Therefore, the Stratux has at least one data point within the 1 second interval of G1000 data. The application stores the data in ‘csv’ format.

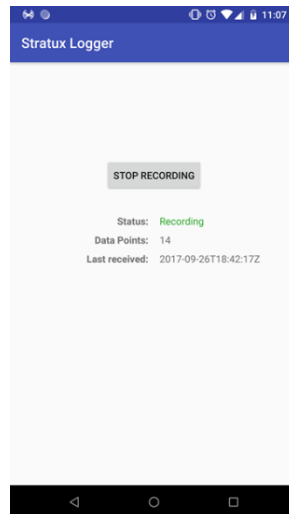


Figure 7: The User Interface (UI) of the Stratux Logger application on the Google Pixel 5

We placed the Google Pixel-5 phone with the Stratux Logger application and the Stratux in the baggage area of three different SR-20 aircraft at Purdue University. Figure 8 shows the Styrofoam

mount on which we placed the Stratux and phone to strap it down to the aircraft. We visually aligned the Stratux longitudinal axis with the aircraft longitudinal axis.



Figure 8: The mount ensures that the location and direction of the equipment is consistent in all flight tests.

The Stratux Logger application collected flight data from 29 training flights. Flights included training aircraft maneuver techniques and cross-country flights. The Stratux does not have an internal power unit. We used an external power bank of 10400 mAh to power the Stratux. The battery lasts for approximately 7 hours per day.

There were some seasonal hindrances to the data collection process. During the winter, the weather was often not suited for training flights. During the summer, the smartphone recording the Stratux data would shut down due to overheating.

An SD card on-board the aircraft recorded the Garmin G1000 data. We downloaded the required files from the SD card. Table 1 contains the differences between the Stratux and G1000 data collected. The differences exist due to our experimental setup (recording time and collection method) and due to the inherent nature of the system (GPS time format and additional sensor data).

Table 1: Differences between the Stratux data collection and the G1000 data collection

Stratux	G1000
Data is recorded throughout the day. A data dump contains multiple flights.	Data is recorded only when engine is turned on. A data dump contains information from engine start to engine shutdown.
Data is recorded every 0.9 seconds.	Data is recorded every 1 second.
GPS time is in UTC.	GPS time is local (EST).
Stratux has no information from aircraft sensors. (E.g.: Engine parameters, IAS). Total of 39 unique flight data variables.	G1000 data contains aircraft sensor data. (E.g.: Engine parameters, IAS). Total of 69 unique flight data variables.

3.2 Stratux Data Processing

We read the G1000 and the Stratux csv files into MATLAB. We created two data structures for the Stratux and the G1000, as shown in Figure 9. Flights contain data points within each variable.

For example, flight 1 has 6003 data points in each variable.

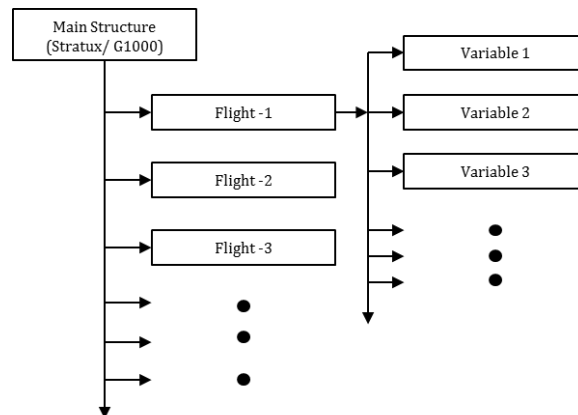


Figure 9: Each data structure contained flight variable information.

For the Stratux, we converted the Zulu time to local time. We added a new variable which provides a common date and time format for the Stratux and the G1000.

3.2.1 Segregating Flights

A single G1000 data file recorded the data from the moment the G1000 was switched on to the time it was switched off. We define a flight as the time between the start time recorded on a G1000 data sheet and the last time on that data sheet. We created substructures of each flight into the main G1000 family of structures. A single Stratux data file recorded data for the entire day. Calculating flight time is complex. Without a reference, the duration or identification of flight can only be based on GPS ground speed or altitude. We read the Stratux data per day and then used the GPS time and date in both the Stratux and the G1000 to identify the corresponding G1000 recorded flights in Stratux. The extra data on the Stratux is useless as it represents the aircraft in an idle state on the ramp and so we discarded it. Similar to the G1000 family structure, we divided the Stratux family structure into the identified flights.

3.2.2 Syncing G1000 and Stratux data

The Stratux and the G1000 have different recording times. Therefore, there were unequal data recordings for the same flight time. Further, both systems have inbuilt errors in recording where the time or information is duplicated. The Stratux also has data recording in milliseconds, whereas the G1000 time accuracy is only to 1 second. We therefore rounded all Stratux times up to the start of each next second using Matlab's "dateshift" function. For all repeated time instances, we only considered the maximum value of the variable data for both the Stratux and the G1000. Since the G1000 is our 'gold standard' we find all the unique times recorded on the G1000 in Stratux for each flight. However, if the Stratux time was missing, then we could not use the corresponding G1000 data for comparison. We snipped the Stratux and the G1000 flight data structures in one-to-one mapping of data which has a mean time difference of 1.0232 seconds between data points per flight. We acknowledge that the syncing and snipping of data may introduce errors, but it is

necessary for valid comparison of the data from two different sources. We attempted rounding the Stratux time up to the next second and taking the mean of variable data of non-unique time recordings but did not see any unreasonable or significant variation in data. From here on, we accepted any errors that may have been introduced and performed our analysis. For the 29 flights, the number of data points in each variable, after data processing, is 115,867.

3.3 Characteristics of the Roll Angle Data from the Stratux and the G1000

As discussed earlier, the variable of interest is the roll angle. Figure 10 shows the processed roll data for the first flight.

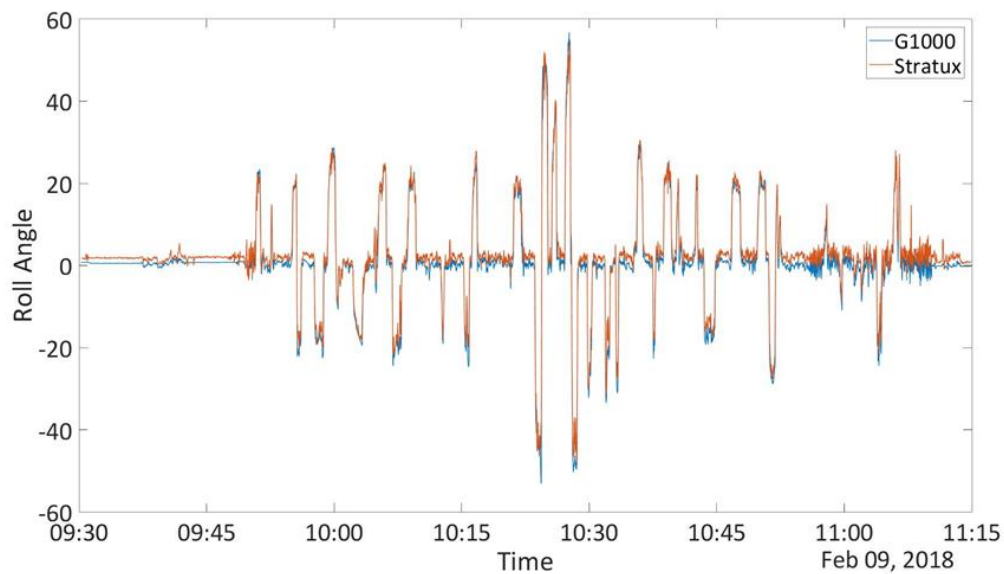


Figure 10: The direction sign associated with the angle is the same in both the G1000 and the Stratux. Right turns are positive and left turns are negative.

3.3.1 Error Definition

The angle error is defined by equation 3. The error is positive when the magnitude of the G1000 roll angle is greater than the magnitude of the Stratux roll angle. To maintain this characteristic of

the error, we modified the error equation with respect to the relative direction of roll between the G1000 and the Stratux.

$$error = \phi_{G1000} - \phi_{Stratux} \quad (3)$$

Table 2 provides the mean and variance of the error for right and left turning angles. We performed 1- way ANOVA test for positive angle errors and negative angle errors. The p-value for the analysis was $2.7329 \cdot 10^{-43}$, thereby proving that the two means are not equal. Thus, we cannot use the absolute value of roll angle to model the Stratux roll angles, since the error for left and right roll angles are statistically different.

Table 2: Mean and Variance of Errors for positive and negative roll angles

	Mean	Variance
Angles ≥ 0 (Right Turns)	0.4275	2.7034
Angles < 0 (Left Turns)	0.2844	3.4963

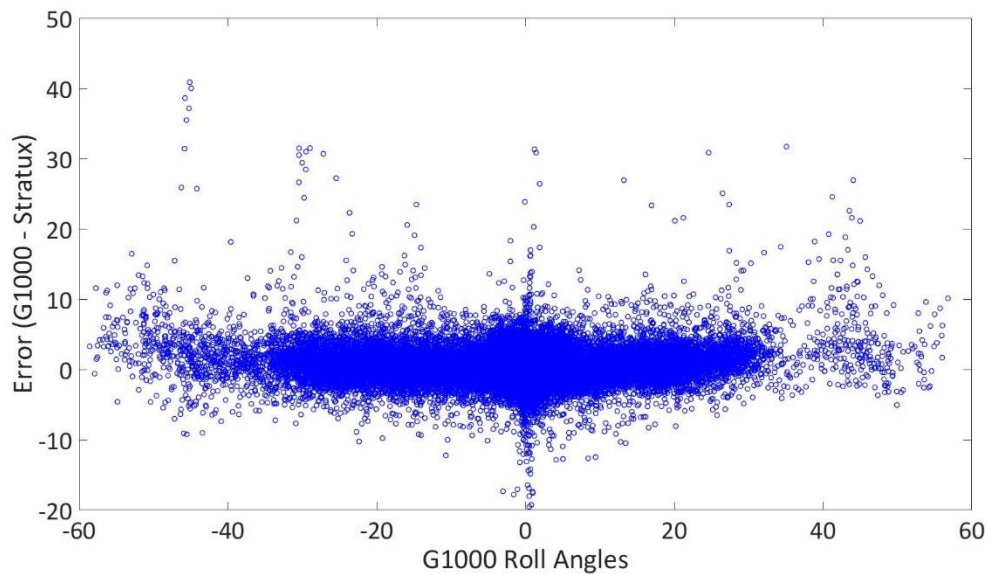


Figure 11: The roll angle error between the Stratux and the G1000 has large variations.

Figure 11 shows the error distribution from all data points with respect to the G1000 roll angles. The error between the Stratux and the G1000 is not symmetric about 0° . A hazardous roll angle limit is the same for positive and negative roll angles. However, this asymmetry means that the error at a positive hazardous roll angle limit is different from the error at a negative hazardous roll angle limit. We show in section 0 how the error helps define hazardous roll angle limits for the Stratux.

3.4 Comparison of the Stratux roll data and the G1000 roll data

In this research, we want to identify if we can use the roll angle data as measured by the Stratux in GA safety analysis, similarly to how we use roll angle data from the G1000. It is therefore necessary to establish if the Stratux roll angle and the G1000 roll angle are different and if the error between them is greater than the standards for a non-gimbal AHRS unit. Figure 12 shows the distribution of data based on angle for all the data points we collected.

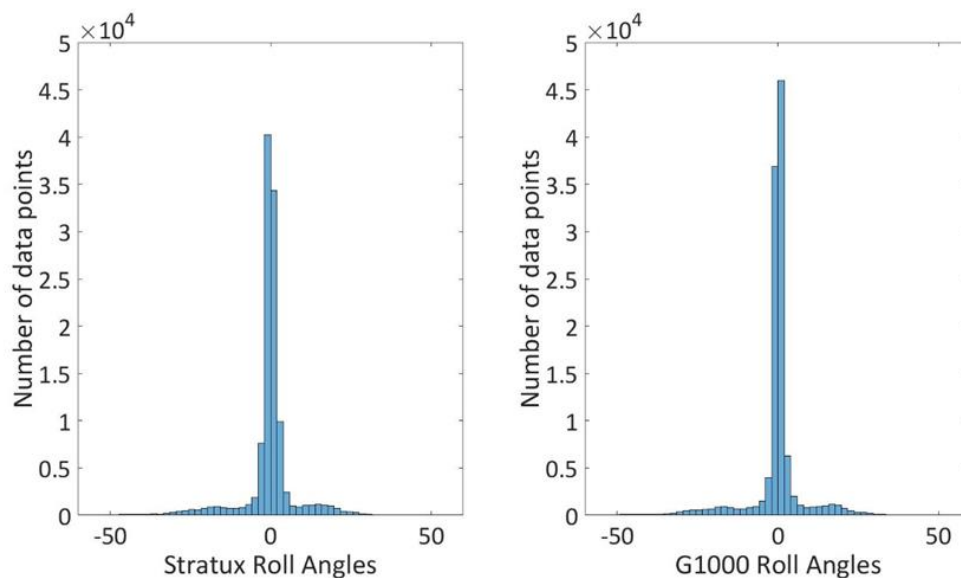


Figure 12: Stratux (Left - a) and G1000 (Right - b) roll data histogram distribution show the large concentration of data in lower magnitude angles

Figure 11 suggests that the Stratux roll angle is erroneous compared to the G1000 roll angle. We need to know whether we have sufficient data points for all angles from -60° to $+60^\circ$ to prove that the Stratux and the G1000 roll angles are not equivalent. We set our null hypothesis as the Stratux roll angles are equivalent to the G1000 roll angles. To define our null hypothesis, we considered the minimum operational performance standards (MOPS) for non-gimbal, on-board AHRS systems.

3.4.1 Standard DO-334

The RTCA DO-334 document provides the MOPS for on-board AHRS. It is intended for equipment that does not use gimballed sensors and for equipment that outputs attitude (pitch and roll) [RTCA DO-334, 2012]. This document describes that strap down AHRS for an aircraft can be of six different categories, A1 to A6. Each category has static and dynamic accuracy associated with it. The lower the category value, the more stringent the accuracy requirement for the strap down AHRS. The highest allowable error is 2.5° for Category A4 and A5 as per FAA TSO C201 [AC No: 20-181, 2014; Krak, 2014].

3.4.2 Power Analysis

If the Stratux roll and G1000 roll are equivalent, then the error between the Stratux and G1000 should have a mean of 0° and a maximum standard deviation of 2.5° . We set the mean error = 0° and a standard deviation of 2.5° as our null hypothesis. However, the error behavior is not the same for the entire range of observable angle as shown in Figure 11. Therefore, we test our null hypothesis for every 5° interval from -60° to $+60^\circ$. We use the data from the first 5 flights as our sample data. The alternate hypothesis is that the G1000 and Stratux roll angles are not equivalent. We use mean error from the sample data at each 5° interval as the alternate hypothesis. We performed a power analysis of power = 0.9 (the probability of the alternate hypothesis being true

given that the null hypothesis is rejected) to determine how many data points we need to establish that the Stratux roll angle is not equivalent to the G1000 roll. If the number of data points we collected from 29 test flights came short of the required data points from the power analysis, then either we need more data to prove the inaccuracy between the Stratux and the G1000, or the Stratux and G1000 roll angles are equivalent for GA safety analysis.

Table 3 shows the required number of data points from power analysis, compared to the number of data points we collected for two intervals of roll angles. The Stratux matches G1000 values more closely at roll angles of lower magnitude than angles of higher magnitude. Therefore, we require fewer data points to reject the null hypothesis at angles of higher magnitude and more data points at lower magnitude. Our power analysis show that we have sufficient data from the 29 flights to prove that the Stratux roll angle and the G1000 roll angle are not equivalent for all angles ranging from -60° to $+60^\circ$.

Table 3: Required number data points from power analysis compared to the number of data points we collected for two intervals of roll angles

Range of Roll Angle	Required Number of Data Points	Data Points we collected from 29 flights
-40° to -45°	22	234
20° to 25°	642	1347

3.4.3 Cross-Correlation and Time Shift between the Stratux and the G1000

We have identified that the Stratux roll angle data and the G1000 roll angle data are not equivalent. The error comparison of the data in sections 3.3.1 and 3.4.2 above is at each data point with no information from nearby points. Roll data for both the Stratux and the G1000 are over a time period. The Stratux may be different from the G1000 because the response from Stratux is either leading (early) or lagging (delay), and the Stratux and the G1000 will be equivalent if the Stratux output

is shifted based on the lead or lag. We therefore need to check if the Stratux and the G1000 have a time difference in between the roll angle outputs.

Cross-correlation is a way of identifying potential correlation between two, time series signals. Figure 13 shows the cross-correlation for all roll angles collected. The lag on the x-axis is the time shift between the two data points from the two signals for which we find the correlation. Lag = 0, is the same data point for G1000 and Stratux, lag = 1 is the next data point on Stratux and so on.

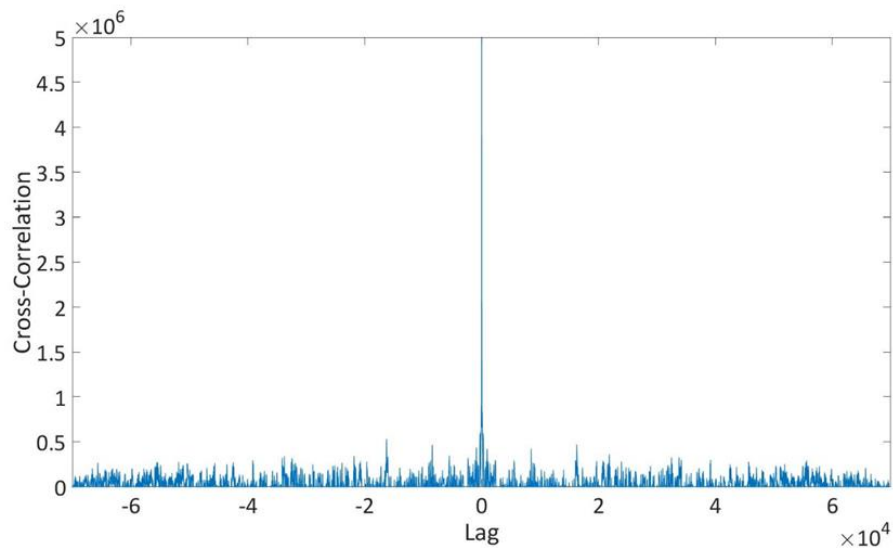


Figure 13: Maximum cross-correlations between the G1000 and the Stratux roll angles occurs at Lag = 0.

In the Figure 13, the maximum cross-correlation occurs at lag = 0, which shows that there is no time shift in the signal between the Stratux and G1000.

3.5 Roll Angle Error Characteristics

Figure 12 shows that we have a lot of data points between -20° and $+20^\circ$. Angles greater than $+40^\circ$ and less than -40° have fewer data points. The error distribution shown in Figure 11 indicates that

the error between the G1000 and the Stratux is not constant, but rather varies depending upon the angle measured.

To find the behavior of the error, we first fit a linear regression model to the error data, as shown by the red line in Figure 14 and equation 4.

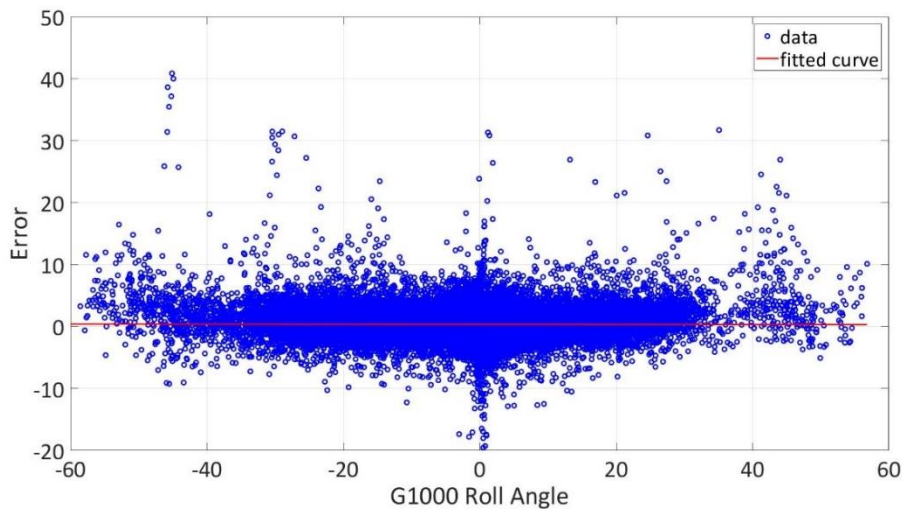


Figure 14: Linear fit for Error vs the G1000 roll angles

$$error_{model} = a \cdot \phi_{G1000} + b \quad (4)$$

Table 4: Co-efficient values of the linear fit for the error

Coefficients	Coefficient Value	95% Confidence Interval
a	-0.000697	-0.001879, 0.0004846
b	0.36741	0.3574, 0.3775

For the roll error to be independent upon the observed angle, the confidence interval of the slope of the fit cannot contain zero. Table 4 shows that the confidence interval of the coefficient of ' a ' includes 0, the fit suggests that the error is independent of the G1000 Roll Angle. That is, the error

is independent of the angle measured. However, the r^2 value ($1.1537 \cdot 10^{-5}$) for the fit is poor and that the result cannot be trusted.

We created 13 intervals of 10° from -65° to $+65^\circ$ and fit linear models to the corresponding errors. Figure 15 shows the linear fits for two of the 13 intervals and Table 5 provides the statistical results of the two linear fits.

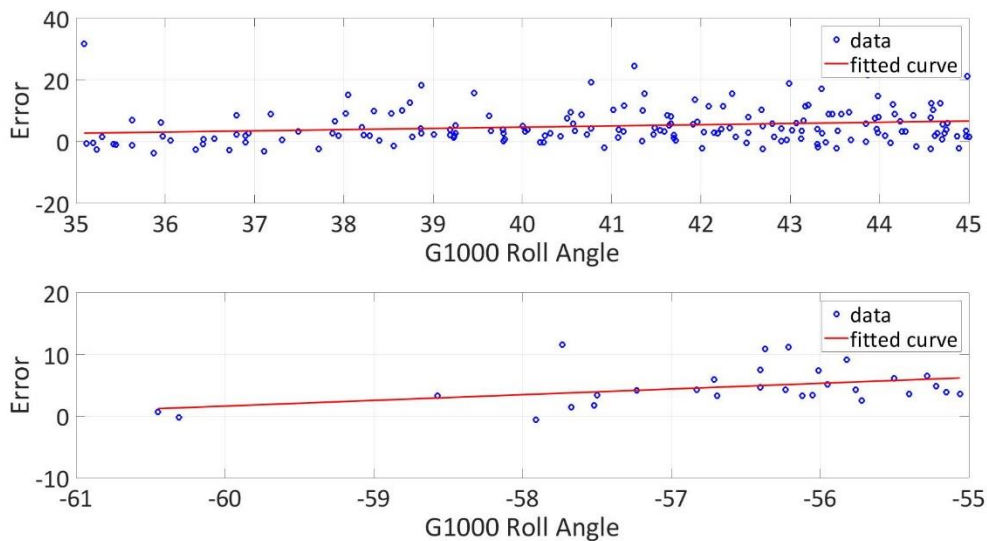


Figure 15: (a) Linear fit of the error for the G1000 roll angle interval of 35° to 45° . (b) Linear fit of the error for the G1000 roll angle interval of -61° to -55° .

Table 5: 95% CI of the slope of the linear fits and the r^2 values, for the two angle intervals shown in Figure 15

Angle Bins	a	95% Confidence Interval	R^2 Value
35° to 45°	0.3974	0.08389, 0.711	0.0341
-65° to -55°	0.9234	0.1192, 1.728	0.1650

The 95% confidence interval of the slope of the linear fits shown in Table 5 indicates that the errors varies with observed angle in the given intervals. Out of the 13 angle intervals, 9 intervals showed

a significance of the angle on the error and 4 indicated independence of error from the angle. Since the error is not uniform for all observed angles, we conclude that Stratux roll output accuracy changes with observed angles.

3.6 Detecting Hazardous Bank Angle

We used the Private Pilot-Airman Certification Standards [FAA, 2018] banking (rolling) maneuvers limit of 45° as the safe roll angle limit to test whether it is feasible to use the Stratux to detect hazardous roll angles in post-flight analysis. We assume that the G1000 roll angle data is an accurate measurement of the actual behavior of the system and we tested whether the Stratux captured the same state as the G1000. If the Stratux roll angle magnitude was less than 45° when the G1000 roll angle magnitude was greater than 45° , then the Stratux had a ‘Missed Detection’. If the Stratux roll angle magnitude was greater than 45° when the G1000 roll angle magnitude was less than 45° , then the Stratux had a ‘False Alarm’. Figure 16 shows that the Stratux data missed nearly half of the hazardous states in flight 1 and flight 7, and almost all the hazardous states in flight 3 and flight 5. We expected the Stratux to perform poorly in detecting hazardous state due to the large errors shown in Figure 11. Therefore we need to either improve the Stratux roll angles or change the definition of the hazardous limit applied to the Stratux to have better detection accuracy when using the Stratux.

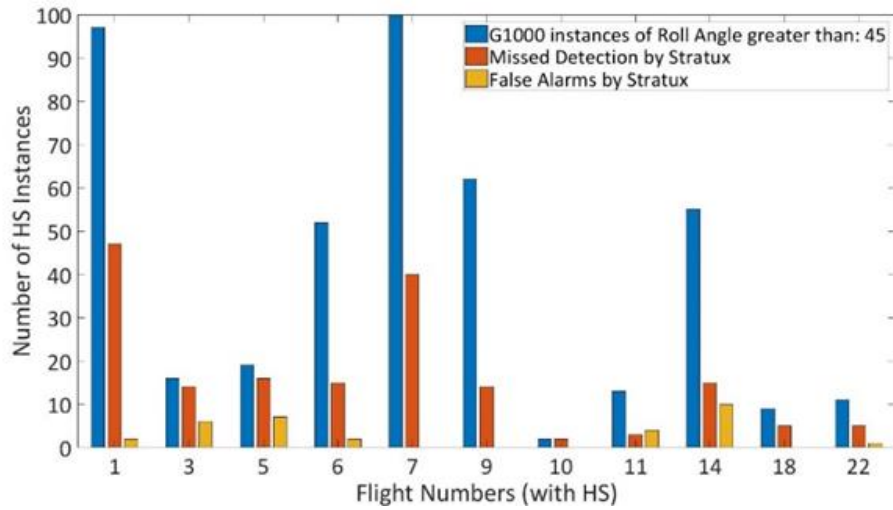


Figure 16: Missed Detections and False Alarms of the Stratux compared to the G1000 for a hazardous roll angle limit of 45°.

3.6.1 Improve Stratux roll angles

To correct the errors in the Stratux angles, we used three different types of models: (1) a continuous linear model that maps the Stratux roll angles to the G1000 roll angles, (2) piecewise transfer functions to model the error and then correct the Stratux roll angles, and (3) piecewise polynomials that map the Stratux roll angles to the G1000 roll angles. In our research, we do not search for the ‘best fit’ model for the Stratux but investigate whether it is possible to improve the detection of higher roll angles using a Stratux device.

3.6.1.1 Model 1: Continuous Linear Model

We used a continuous linear model to improve Stratux roll angle as shown by equation 5. Figure 17 shows the linear function that fits the Stratux roll angle data to the G1000 roll angle data.

$$\phi_{G1000} = a * \phi_{Stratux} + c \quad (5)$$

The coefficients a and c characterize the linear model. $a = 1.009$ and $c = 0.1276$ provided a fit with an $RMSE$ value of 1.7762 and $r^2 = 0.9563$. Statistically, one would consider the fit to be a good fit.

However, the Stratux and G1000 roll data have an unequal distribution of data recorded for all roll

angles. We have more data points for lower magnitude roll angles than for higher magnitude roll angles. The statistical results of the linear fit can be attributed to the large number of data points at the lower magnitude angles.

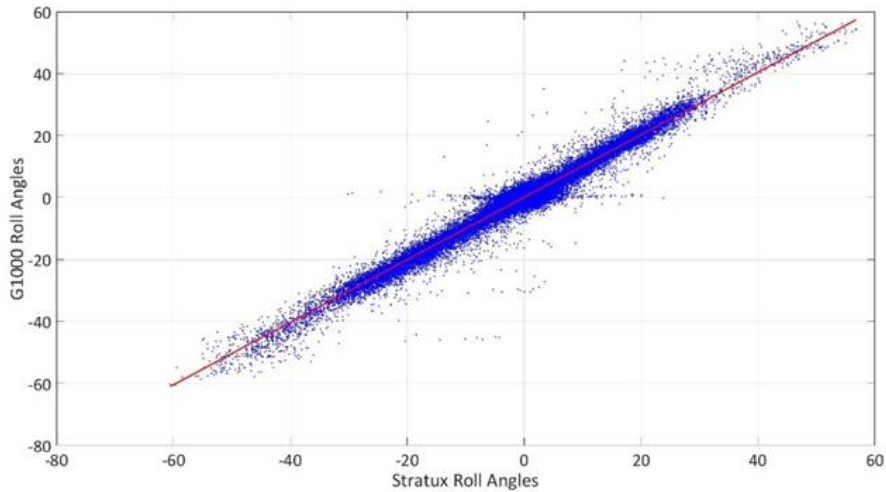


Figure 17: Single Linear Model of the G1000 roll angle from the Stratux roll angles

3.6.1.2 Model 2: Error Model for Stratux Roll Angles using piecewise Fourier Transfer

We split the range of the Stratux roll data into thirteen intervals from -65° to $+65^\circ$ of 10° each. Since our goal is to correct Stratux errors, we use the Stratux roll angles to create the intervals rather than the G1000. We model the error as a function of the Stratux roll angle for each interval. Models for each interval are independent of the other, piecewise, and discontinuous. Equation 6 shows the Fourier transfer function type that captures the error characteristics. The number of function parameters varies based on the interval for which we chose the model.

$$error_{G1000} = a_0 + a_1 \times \cos(w \times \phi_{Stratux}) + b_1 \times \sin(w \times \phi_{Stratux}) + \dots \quad (6)$$

In equation 7, we add the improved error back to the observed Stratux angle to find the improved Stratux roll angle:

$$\phi_{G1000} = \phi_{Stratux} + error_{G1000} \quad (7)$$

Figure 18 shows the error models for the thirteen intervals. The amplitudes of the transfer functions are higher at higher magnitude roll angles because the error variations are large and because of the lack of data at very high angles.

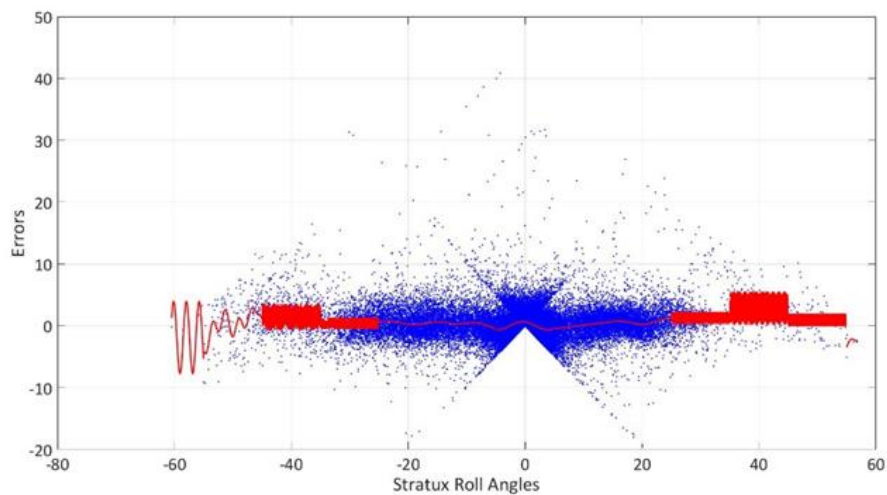


Figure 18: Models for the Error from 10° intervals of the Stratux roll angles

3.6.1.3 Model 3: G1000 Roll Angle Model for Stratux Roll Angles using piecewise Polynomial functions

With model 3 we modify the Stratux roll to directly mimic the G1000 roll angles; unlike model 2 where we used the error to find the improved Stratux indirectly. Similar to model 2, we split the Stratux roll angles into thirteen intervals from -65° to $+65^\circ$ of 10° each. Equation 8 shows the polynomial function type for each of the thirteen intervals. As with model 2, all polynomial models for each interval are independent of each other, piecewise and discontinuous. The number of parameters varies based on the interval for which we chose the model. Figure 19 shows the thirteen

models for each interval. The number of parameters of the polynomial increase for higher magnitude angles due to high error and lack of data points.

$$\phi_{G1000} = p_0 + (p_1 \times \phi_{Stratux}) + (p_2 \times \phi_{Stratux}^2) + (p_3 \times \phi_{Stratux}^3) + \dots \quad (8)$$

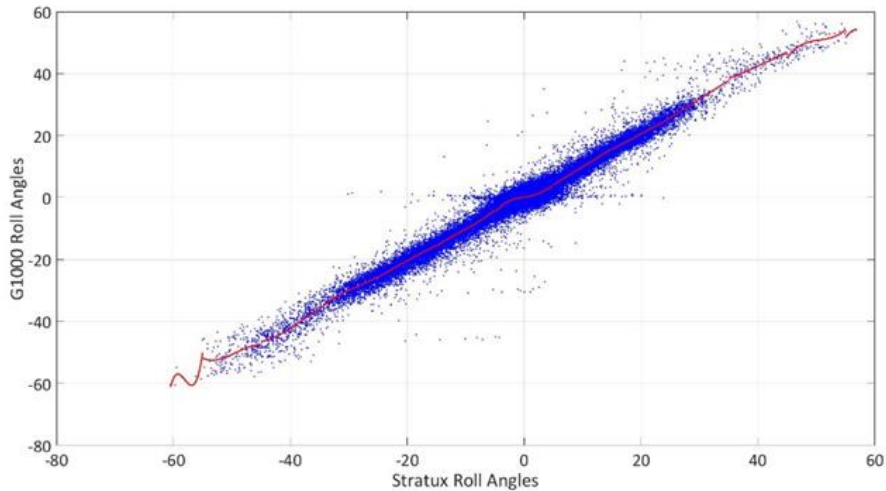


Figure 19: Models for the G1000 roll angles from 10° intervals of the Stratux roll angles

3.6.1.4 Results on Training Set

We created the models using the roll angle data from a random selection of 24 flights (training data set) out of the 29 flights. We reserve 5 flights to test the models (test data set) later in section 5. Table 6 shows a comparison of ‘Missed Detections (MD)’ and ‘False Alarms (FA)’ between original Stratux values and the three models discussed above for all flights having at least one instance of the hazardous state (HS). Model 1, despite being a statistically good fit, does not improve detection of high roll angles. Model 1 cannot improve the Stratux roll angle values at high magnitude angles and thus cannot detect the hazardous states. Model 2 and Model 3 both improve upon the missed detections, but also increase false alarms. Since in Model 2 and Model 3, different implementations and function types gave similar results, we conclude that piecewise models

reduce missed detections but increase false alarms. Since the piecewise models show improvements, we choose Model 3 for further investigation.

Table 6: Comparison of Missed Detections (MD) and False Alarms (FA) between the actual Stratux roll angle data and three models to improve the Stratux roll angles on training data set.

No. of Flights with HS ($\phi_{G1000} > 45^\circ$)	Actual Stratux Roll Angle Data		Model 1: Continuous Linear Fit		Model 2: Piecewise Fourier Transfer Function Model		Model 3: Piecewise Polynomial Function Model	
	MD	FA	MD	FA	MD	FA	MD	FA
1	47	2	42	4	29	14	27	13
2	14	6	13	9	8	25	8	26
3	16	7	16	7	12	17	12	20
4	15	2	15	2	11	3	11	3
5	40	0	39	0	21	3	21	3
6	14	0	12	0	3	0	5	1
7	2	0	2	0	0	1	0	1
8	15	10	14	14	7	19	9	22
9	5	0	2	0	0	1	0	1
10	5	1	5	1	2	3	1	3

3.6.2 Changing Roll Angle Safety Limit for Stratux

For comparing the roll angle detection accuracy of the Stratux to the G1000 we used 45° as our roll angle limit. This limit is a ‘hard’ limit, in that there is no error buffer. For example, if the G1000 angle was 45.1° and the Stratux was 45° , we would consider the Stratux to have missed the detection. We also know that the Stratux roll angles are erroneous compared to the G1000 roll angles. Therefore, if we use a hard limit for the G1000, we must consider a ‘zone of uncertainty’ about that angle when applying the limit to the Stratux. We refer to these adjusted limits as the ‘soft’ limits.

We used the error samples at every 1° interval of the G1000 roll angles ranging from -60° to $+60^\circ$ to find the mean error at each interval. Equation 9 defines the hazardous state limits for Stratux (soft limits):

$$\textit{Soft Limit} = \textit{Hard Limit} \pm \mu_{\textit{Error}} \quad (9)$$

Using equation 9, we redefine the ‘Missed Detection’ and ‘False Alarm’ errors based on the soft limits for $+45^\circ$ and -45° :

- If the G1000 roll angle magnitude is greater than $|45^\circ|$ and the Stratux roll angle magnitude is less than $|45^\circ|$, but greater than the magnitude of the “inner” soft limit (lower magnitude limit), then we cannot say for certain that the Stratux missed detecting a hazardous state.
- If the G1000 roll angle magnitude is less than $|45^\circ|$ and the Stratux roll angle magnitude is greater than $|45^\circ|$, but less than the magnitude of the “outer” soft limit (higher magnitude limit), then we cannot say for certain that the Stratux has falsely detected a hazardous state.

Figure 20 shows the instances of all angles greater than 43° in flight number 5. For ease of visualization, we have removed time from the x-axis and so each instance is not equally spaced in time. We chose 43° to have a zoomed-in view of instances near the hazardous state. The solid black lines indicate the hard limits and the dashed black lines indicate the soft limits. We refer to the lower magnitude limits as the ‘inner soft limit’ and the higher magnitude limits as the ‘outer soft limit’. Since the error distribution is not symmetric about 0° , the same hard limit for negative and positive roll angles has different soft limits for the Stratux. The zones of uncertainty are marked by translucent red bands. We consider the Stratux angles that lie within the red bands as correct detections.

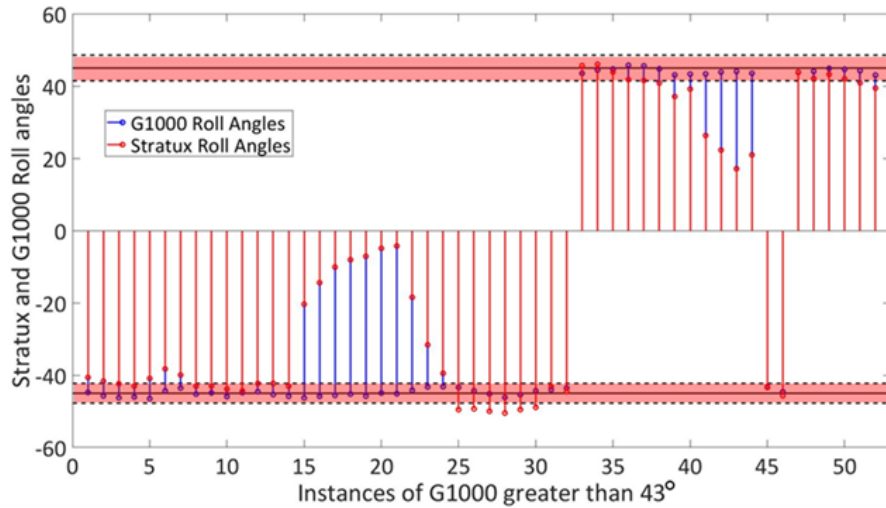


Figure 20: Change of Hard limits to Soft (Red Bands) Limits for the Stratux for an example flight data.

Figure 21 shows the results for missed detections and false alarms, similar to that of Figure 16. However, in the case of Figure 21 we use the actual Stratux and the soft limits, resulting in a decrease in missed detections and false alarms.

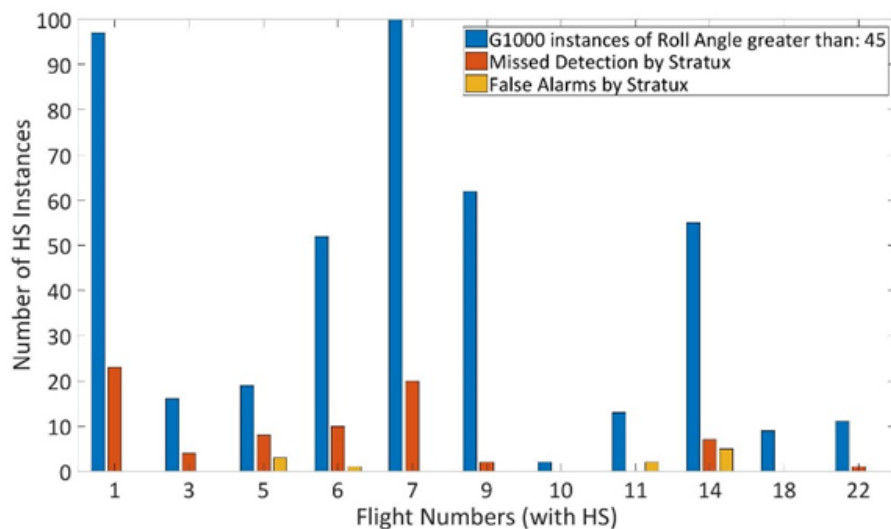


Figure 21: Missed Detections and False Alarms of actual Stratux roll angles compared to the G1000 roll angles when we use soft limits of 45°.

3.6.3 Probability of Detecting Hazardous State ($\phi > 45^\circ$)

We find two types of hazardous detection probabilities: (1) The probability of the Stratux correctly detecting a hazardous state given a G1000 hazardous state and (2) the probability of a G1000 hazardous state occurring given a Stratux angle. These two probabilities give us an idea about the relative accuracy of hazardous state detection using the Stratux compared to the G1000.

3.6.3.1 Probability of our Stratux detecting a G1000 Hazardous State

We treat the detection of hazardous states as discrete independent events, where a detection is a success and a missed detection or false alarm is a failure. We use equation 10 to find the correct detections (CD) of hazardous state. If the Stratux roll angle is able to correctly identify all the instances of the G1000 hazardous states but has additional false alarms, then the CD of the Stratux drops. Previous studies have shown that nuisance alarms can decrease user trust in the system, or lead to operators ignoring the alarms [Cafarelli, 1998; William, 1998].

$$CD = (Instances\ of\ HS)_{G1000} - MD_{Stratux} - FA_{Stratux} \quad 10$$

We find the probability of Stratux correctly detecting a hazardous state (HS) given that a hazardous state has occurred in reality (according to the G1000), i.e. $p(HS_{Stratux} | HS_{G1000})$. We find the 95% confidence interval of the probability using the Clopper-Pearson method [Clopper and Pearson, 1934]. When we use the actual Stratux roll angles and the hard limit of 45° , the probability of detection for the Stratux is 0.5229 with a 95% confidence interval of 0.4749 – 0.5707. We also evaluate the probability of correctly detecting a hazardous state using the improved Stratux or the soft limits for the Stratux in section 5.1.

3.6.3.2 Probability of Hazardous State occurring at Stratux Angles

Since the Stratux error varies with angle, the probability of observing a hazardous state for a given Stratux angle also varies. Here, we find the probability of a hazardous state (HS) occurring (according to G1000) for an observed Stratux angle, i.e. $p(HS_{G1000} | \phi_{Stratux})$.

For example, if the Stratux records an angle of 40° , and the defined limit is 45° then the possibilities are:

- The G1000 roll angle is greater than $+45^\circ$ or less than -45° and a hazardous state has occurred.
- The G1000 roll angle is less than $|45^\circ|$ and no hazardous state has occurred.

We developed the PDFs of the G1000 roll angles for a 1° range of the Stratux roll angles spanning from -60° to $+60^\circ$. Figure 22 shows the PDF for $+40^\circ \leq \phi_{Stratux} < +41^\circ$ and the area under the curve for a hazardous state ($\phi > |45^\circ|$).

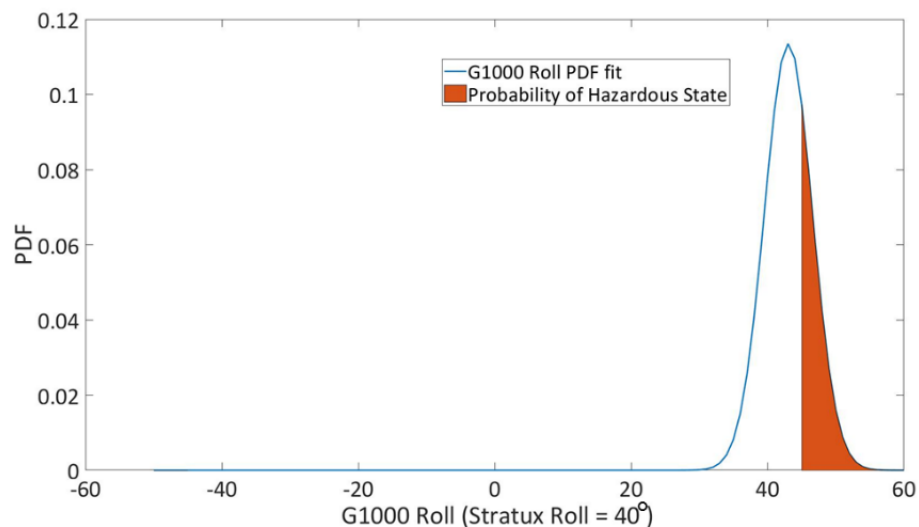


Figure 22: G1000 Roll Angle PDF for the actual Stratux roll = 40° and the area under the curve beyond hard limit of 45° is the probability of HS.

In Figure 23, the solid red line indicates the ‘Ideal Probability’ of detecting the hazardous state. It is zero (0) between -45° and $+45^\circ$ and one (1) beyond the limits. The probability of a hazardous state for a given Stratux angle (40° in Figure 22) is the area under the PDF in Figure 22. The blue line with markers in Figure 23 is the probability for each Stratux angle based on the flight data. The probability for hazardous state is the sum of CDF for -45° and $(1 - \text{CDF})$ for $+45^\circ$.

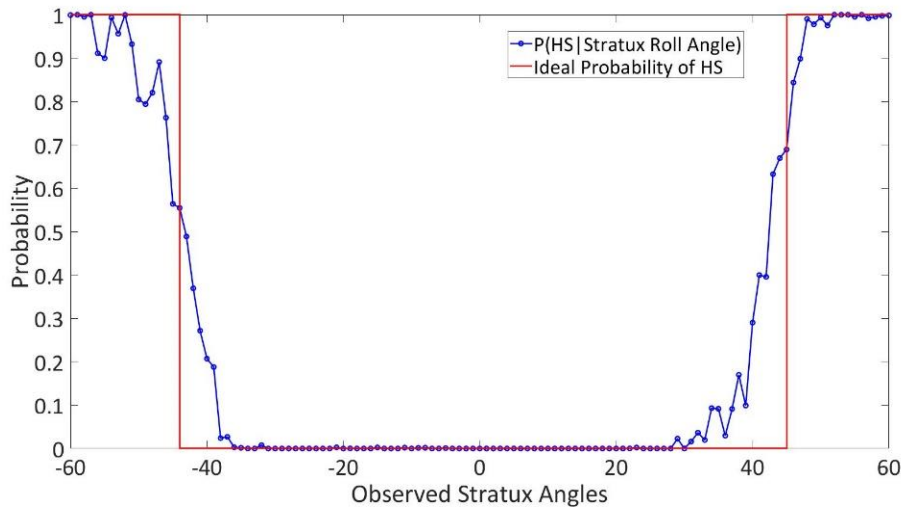


Figure 23: Probability of HS occurring for all Stratux Angles

4. DETECTING ACCURACY FOR TIME ALONG WITH ANGLE

For time accuracy, we have already established that there is no lag or lead in roll angle output between the Stratux and the G1000 (Section 3.4.3). Due to incorrect detection of high angles, there is incorrect detection of time spent in the high roll angle hazardous state. While in the high roll angle hazardous state ($\phi > 45^\circ$), risk increases for higher magnitude angles or for longer time spent in the hazardous state. Therefore, it is important to analyze the time accuracy along with the angle accuracy of a low-cost system such as the Stratux.

In this section we evaluate the time and angle accuracy of the Stratux beyond the hazardous angle limit of 45° . To perform an accuracy analysis on both angle and time, we first need a function of angle and time. We refer to such a function as ‘Risk Level’. The function of ‘Risk Level’ remains the same for the Stratux and the G1000. Equation 11 shows the representation of risk level as a function of angle (ϕ) and time (t):

$$\text{Risk Level} = f(\phi, t) \quad 11$$

4.1 Definition of Risk Level (RL)

To define risk level, we first need to define a ‘risk ladder’ [cf. Sandman et al., 1994]. A risk ladder describes the risk level from the lowest level to the highest level. Since aircraft accident causality cannot be purely attributed to single factors such as a high roll angle, for our research purpose we set the lowest value of risk level to 0 and highest value of risk to 100. Hunter (2006) used a similar risk ladder in evaluating risk perception in GA pilots. Risk level 0 indicates straight and level flight and risk level 100 indicates that the aircraft was at a roll angle 15° greater than the hazardous roll angle limit for 5 minutes or more. Since our hazardous roll angle limit is 45° , the maximum risk

level occurs when an aircraft exceeds 60° roll angle for 300s. For the Cirrus SR20, the maximum allowable roll angle for any maneuver is 60° [Cirrus POH, 2003]. Hunter (2002) found that pilots perceive a 45° high roll angle on the final approach to have a mean risk level of 67.2 and standard deviation of 17.4 for risk level ranging from 0 to 100. A study concerning perceived risk showed that for a given state, the perceived threat increases for a higher displaced location of risk level value on the risk ladder [Sandman et al., 1994]. Keeping in mind previous studies for pilots' risk understanding [Hunter, 2002] and human risk perception [Sandman et al., 1994], we define the risk level to be 60 when roll angle value recorded exceeds the hazardous roll angle limit (45°) by one second.

4.2 Definition of Risk Category (RC)

The risk level in the previous section characterizes risk as a function of roll angle and time. The higher the roll angle magnitude or the longer the time, the higher the risk level will be. An FAA study used color coded risk gradients to evaluate GA pilots' perception of risk associated with weather information because numerical risk values were confusing to many pilots [Knecht and Frazier, 2015].

To provide simpler feedback than risk level values, we created four risk categories from the risk level values. Risk Category 0 (No Risk) indicates normal aircraft operation. Risk Category 1 (Minor) indicates the operations beyond the hazardous roll angle limit for a short duration. Risk Category 2 (Moderate) and Risk Category 3 (High) indicate operations well beyond the limit angle of 45° or operations in the hazardous state for long durations [ACS, 2018]. In our research we want to evaluate the risk category detection of the Stratux compared to the G1000 for any given

demarcation of risk category on a risk ladder. Figure 24 shows our choice of the demarcations of the risk categories based on the risk level (RL) values.

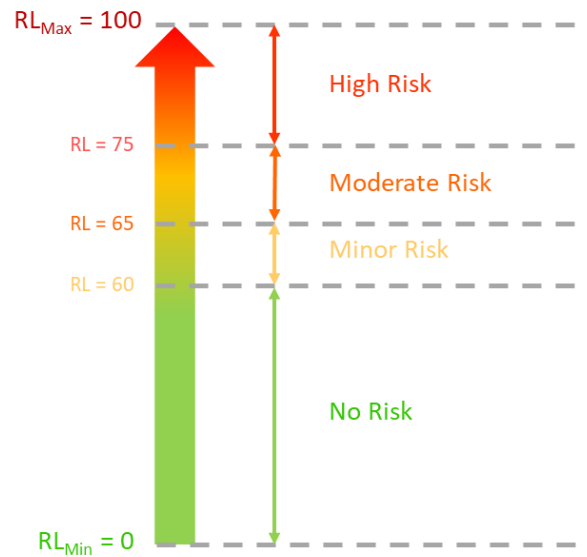


Figure 24: Our choices for RC demarcations based on RL

The RC is ‘Minor’ when the RL = 60, i.e. when the recorded roll angle crossed the hazardous limit of 45° for 1 second.

4.3 Risk Level Functions

To apply the definitions of risk level and risk category we define risk level functions. We use these functions to map the data from the Garmin G1000 and the Stratux to the risk level and the risk category definitions. In our research, we do not aim to find the ‘best’ risk level definition but test whether the Stratux captures the same risk categories as that of the G1000 (Section 4.4) for two different approaches to define the risk level function. We define the risk level function in two ways:

- We integrate the angle with respect to time and assign the integration value to all data points lying within the integration.

- We use a predefined function to find the risk level at a given data point as function of the angle at the data point, and time accumulated at the data point.

4.3.1 Integration of Angle over Time

A simple way to capture both angle and time is to find the integral value of angle with respect to time. As shown in Figure 25, the roll angle is above the hazardous angle between time t_{start} and t_{end} . The risk level is the hashed area under the red curve. Equation 12 gives the risk level (RL) assigned to all data points between t_{start} and t_{end} : The ‘ Δt ’ is the time difference between consecutive data points.

$$RL_{(t_{start}, t_{end})} = \sum_{t_1}^{t_2} \frac{|\phi_t| + |\phi_{t-1}|}{2} \times \Delta t \quad (12)$$

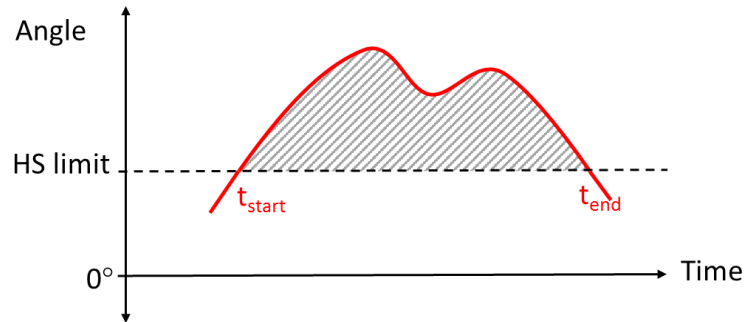


Figure 25: Risk Level between t_{start} and t_{end} is the result of integration of the angle over time.

The resulting integration is always positive because we use the absolute value of the angles. We scale the integration results to fit the definitions of risk level and risk categories. Table 2 shows our choices for the range of integration results (IR) to the corresponding risk levels and risk categories. The table also provides the physical meaning of the aircraft flight behavior corresponding to the values of integration results, risk levels and risk categories.

Table 7: Scaling Integration Results (IR) to risk level and risk category definitions.

IR Scaling Limit Ranges	Risk Level Range	Risk Category Value	Physical Meaning
$IR_{min} = 0$ to $IR_{limit1} = 45$	0 to 60	No Risk (Risk Category = 0)	Level flight to limit angle of 45° exceeded for 0s.
$IR_{min} = 45$ to $IR_{limit2} = 360$	60 to 65	Minor (Risk Category = 1)	Limit angle of 45° exceeded for 1s to exceeding for 8s.
$IR_{limit2} = 360$ to $IR_{limit3} = 900$	65 to 75	Moderate (Risk Category = 2)	Limit angle of 45° exceeded for 9s to exceeding for 20s
$IR_{limit3} = 900$ to $IR_{max} = 18,000$	75 to 100	Major (Risk Category = 3)	Limit angle of 45° exceeded for 21s to 60° exceeded for 300s.

Since all data points between t_{start} and t_{end} in Figure 25 have the same integration results, they also have the same risk level and risk category values.

Figure 26 shows the comparison of risk levels (a) and risk categories (b) of the Stratux and the G1000 data from the first flight test. In Figure 26 (a) the orange plot lines are the risk level values, the blue lines with markers are the G1000 roll angles and the red lines with marker are the Stratux roll angles. In Figure 26 (b) the yellow bars indicate ‘Minor Risk’, the orange bars indicate ‘Major Risk’ and the red bars indicate ‘High Risk’. The blue line with markers indicate both the Stratux and the G1000 roll angles. We used equation 11 to obtain the risk levels. The risk levels are the absolute values of the roll angle till the hazardous angle limit, and beyond the limit we integrate the angle with time. The horizontal straight sections of the risk level graph at high magnitude roll angles indicate data points containing the same risk levels. Within the time span when the roll angle data is beyond the hazardous roll angle limit, the risk categories do not decrease and are all identical due to the same risk level values.

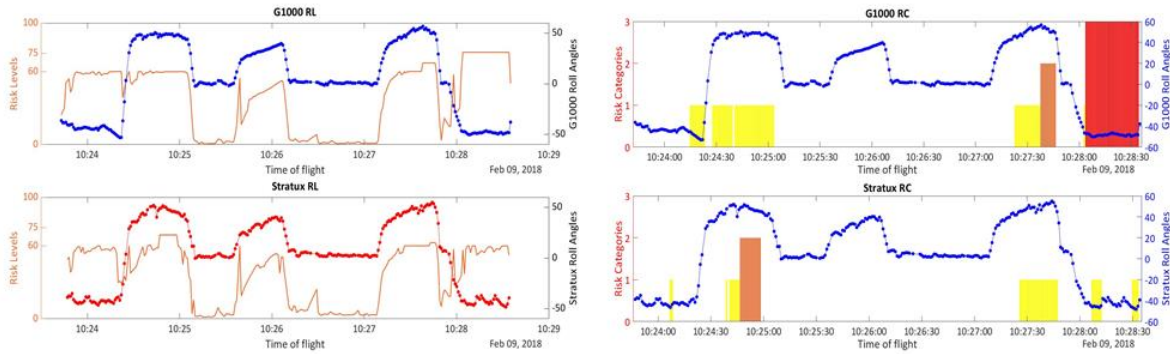


Figure 26: Comparison of risk level (Left – a) and of risk category (Right – b) from the Stratux and the G1000 when we use the integration of angle over time to find the risk level values

4.3.2 Two Risk Level Mapping functions

In the case of integration of angle and time, all the data points between t_{start} and t_{end} in Figure 25 have the same risk level. For the data points to have varying risk level values, we need to compute the risk level at each data point and for that we can use a predefined function of angle and time. Each data point contains angle information but no time information. Instead of integrating with respect to time, we add time information to the data points.

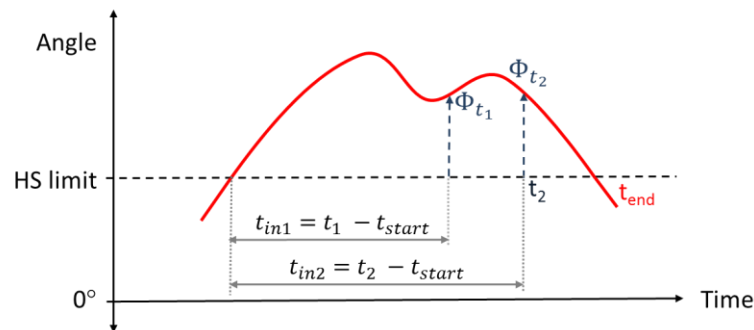


Figure 27: Increment time information for computing varying risk level

In Figure 27 the risk level varies for all the points between t_{start} and t_{end} . For example, the risk level at t_1 is a function of angle at t_1 (ϕ_{t1}) and incremented time at t_1 (t_{in1}) and the risk level at t_2 is a

function of angle at t_2 (ϕ_{t2}) and incremented time at t_2 (t_{in2}). We increment time if the data point crosses the hazardous roll angle limit value. We also increment time for angles below the limit but are bound to the maximum limit of 300 seconds. Table 8 provides the logic for incrementing time beyond the hazardous roll angle limit. ‘Time step’ is the time difference and ‘Angular Step’ is the angular difference between consecutive data points respectively.

Table 8: Logic of incrementing time and risk level at data points

Time Step	Angular Step	Time Allocated to data point
>10s	> 5°	$t_{in} = 1s$
>10s	$\leq 5^\circ$	$t_{in} = 1s$
$\leq 10s$	> 5°	$t_{in} = \text{Time Step}$
$\leq 10s$	$\leq 5^\circ$	$t_{in} = t_{in} \text{ at previous data point} + \text{Time Step}$

Since the function of risk level is predefined, we do not require any scaling. The predefined function is limited to risk level limits of 0 and 100. We assign the risk category to each data point based on the risk level value.

Equation 13 and equation 14 show two risk level functions we chose to map the roll angle and time to risk levels. We did not investigate for the ‘best’ possible function but chose two arbitrary different mapping function to compare the Stratux and the G1000 risk level outputs. In each mapping, the risk level increases linearly with angle. In equation 13, the risk level is exponential with respect to time and in equation 14, the risk level is quadratic with respect to time.

$$RL_i = x_1 \cdot \phi_i \cdot e^{x_2 \cdot t_{in_i}} \quad (13)$$

$$RL_i = (x_1 \cdot \phi_i) + (x_2 \cdot t_{in_i})^2 \quad (14)$$

We fit x_1 and x_2 in equation 13 and equation 14 to the risk level limits discussed before to limit the functions' maximum and minimum values to the risk level limits. The subscript 'i' indicates each data point since we find the risk level at each data point.

Similar to Figure 26, Figure 28 shows the comparison of risk levels (a) and risk categories (b) of the Stratux and the G1000 data from the first flight test. We used equation 14 to obtain the risk levels. Each data point contains a unique risk level assigned by the mapping function. Since the risk levels vary, the risk categories also vary. In the time span the roll data is beyond the hazardous limit angle, the risk categories can vary if the increment time or the magnitude of the roll angle varies.

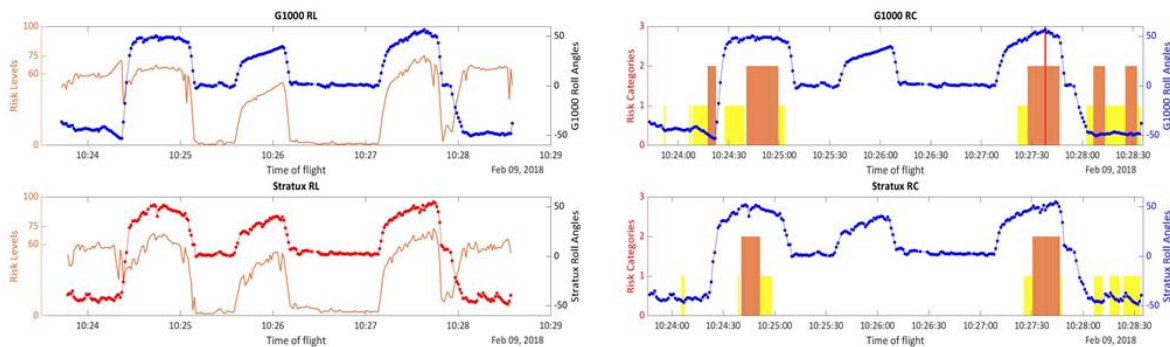


Figure 28: Comparison of risk level (Left – a) and of risk category (Right – b) from the Stratux and the G1000 when we use a predefined mapping function to find the risk level values

4.4 Comparison of Risk Categories between the Stratux and the G1000

When detecting hazardous states purely based on roll angle (Section 3.6), the Stratux could either succeed or fail in detecting states compared to the G1000. For risk categories, the Stratux may have partial failures. For example, if the G1000 risk category is 'High Risk', the Stratux risk category can be 'High,' 'Moderate,' 'Minor,' or 'No Risk.' Of the four possible risk category

detections, only ‘No Risk’ is a complete failure of detection. We evaluated the accuracy of the Stratux in detecting the discrete risk categories obtained from the risk levels, compared to the G1000. Similar to section 3.6.1.4, we use the data from the same 24 randomly selected flights. In this section we use the actual Stratux values and the ‘hard’ limit of 45° in determining the risk level and risk categories. We evaluate the impact of the modelled Stratux values and the soft roll angle limits in section 5.

Table 9, Table 10, and

Table 11 show the conditional probabilities of the Stratux risk category detection

(i.e., $p(RC_{Stratux} | RC_{G1000})$) when we used equation 12, equation 13 and equation 14 to

compute the risk levels respectively. All the columns in each table add up to 1. The green cells in the tables indicate the exact detection probabilities, the yellow and the orange indicate partial detection probabilities, and the red cells indicate complete failure probabilities. Ideally, if the Stratux and the G1000 had the same risk category detections, then the matrices would be 4x4 identity matrices.

Table 9: Conditional Probabilities of the Stratux RC matching the G1000 RC for RL derived from equation 12

		G1000			
		No Risk	Minor Risk	Moderate Risk	High Risk
Stratux	No Risk	0.9995	0.3608	0.1159	0.2556
	Minor Risk	0.0005	0.6157	0.7391	0.2167
	Moderate Risk	0	0.0235	0.1450	0.3722
	High Risk	0	0	0	0.1556

Table 10: Conditional Probabilities of the Stratux RC matching the G1000 RC for RL derived from equation 13

		G1000			
		No Risk	Minor Risk	Moderate Risk	High Risk
Stratux	No Risk	0.9998	0.6483	0.1976	0
	Minor Risk	0.0002	0.2924	0.3202	0.0690
	Moderate Risk	0	0.0593	0.4704	0.7586
	High Risk	0	0	0.0118	0.1724

Table 11: Conditional Probabilities of the Stratux RC matching the G1000 RC for RL derived from equation 14

		G1000			
		No Risk	Minor Risk	Moderate Risk	High Risk
Stratux	No Risk	0.9997	0.6420	0.1853	0
	Minor Risk	0.0003	0.2757	0.3147	0.0588
	Moderate Risk	0	0.0823	0.4871	0.7647
	High Risk	0	0	0.0129	0.1765

The risk levels from the predefined functions (equations 13 and 14) produce lower number of ‘High risk’ categories than the risk levels generated from equation 12, and the Stratux has zero complete failure probabilities.

Table 10 and

Table 11 have similar conditional probabilities. Irrespective of the mapping function we used, the risk categories did not change when using the same roll angle and time data. However, in the future, we would want to further evaluate the extent of change of risk categories with a larger variety of risk level mapping functions.

5. RESULTS: USING THE MODELLED STRATUX AND SOFT LIMITS TO IMPROVE DETECTIONS

In this section, we use the improved Stratux roll angles that we developed in section 3.6.1.3 and the soft limits for the Stratux that we developed in section 0 to find (1) the probabilities of hazardous roll angle detection (similar to section 3.6.3.1) and (2) the probabilities of risk category detection (similar to section 4.4). We test our approach on data from 5 flights that we did not use to build the models earlier to improve the Stratux roll angles or to determine the soft limits of the Stratux.

5.1 Detection of Roll Angles above a Defined Hazardous Limit

We had only 13 instances of hazardous states ($\phi > 45^\circ$) in the data from the 5 test flights. Table 12 shows the number of missed detections (MD), false alarms (FA), and correct detections (CD) for the actual and improved Stratux, and for the hard and soft limits.

Table 12: Comparison of missed detections (MD), false alarms (FA) and correct detections (CD) for the actual and improved Stratux, and for the hard and soft limits for the Stratux when the hazardous angle limit is 45° .

Actual Stratux and Hard Limit			Improved Stratux and Hard Limit			Actual Stratux and Soft Limits			Improved Stratux and Soft Limits		
MD	FA	CD	MD	FA	CD	MD	FA	CD	MD	FA	CD
3	4	6	0	7	6	0	1	12	0	2	11

The improved Stratux roll angles reduce the number of missed detections but increase false alarms by the same amount, thereby not improving upon the correct detections of the Stratux. The soft limits improve correct detection.

Our purpose here is to assess how well our method detects anomalous behavior. Given that our data is all from supervised training flights, we have few instances of roll angles with magnitude

greater than 45° . Solely for testing our method, we define a new hazardous roll angle limit based on anomalous behavior in our test data set. This approach is similar to how unstable approaches are defined [Jiao et al., 2018]. Since we assess the anomalous behavior in the test data set, we only use the test data to find the new limit instead of the complete data set.

We find the magnitude of the 95th percentile of all roll angles in the 5 test flights. For our test data set, that value is 19° . That is, 95% of the roll data is at or below an absolute value of 19° . Thus, we set the new hazardous limit to 19° .

We find the probabilities of the Stratux correctly identifying roll angles having a magnitude greater than 19° using the methods described in section 3.6.3.1. Table 13 shows the probabilities of detection of roll angles greater than 19° for the actual and improved Stratux, and for the hard and soft limits. As shown in section 3.4.2 and section 3.5, the Stratux roll angle error varies, but the error is lower at lower magnitude angles than at higher magnitude angles. Since the hazardous limit we are using here is smaller than the previous limit of 45° , the probability of detection for the actual Stratux is higher than the value of 0.52 we found in section 3.6.3.1. The values in Table 13 also indicate that the model improved Stratux roll angle has little impact on overall correct detection. The soft limits, however, increase the detection probability by 10%.

Table 13: Probabilities of Detection of $|\phi| > 19^\circ$

	Hard Limit and Actual Stratux	Hard Limit and Improved Stratux	Soft Limits and Actual Stratux	Soft Limits and Improved Stratux
Probability of Correct Detection	0.8308	0.8333	0.9160	0.9336
95% CI of Probability	0.8030 – 0.8562	0.8056 – 0.8585	0.8946 – 0.9343	0.9140 – 0.9499

Since many data points are about 0° , we find the 95th percentile of roll data (in test data) with magnitude greater than 10° . The resulting roll angle is 37° . We find the probabilities of correct detection of all angles greater than $|37^\circ|$. Table 14 shows results similar to that of Table 13, but here the improved Stratux roll angles decrease the detection probabilities for hard and soft limits. Applying soft limits still increases the correct detection probabilities.

Table 14: Probabilities of Detection of $|\phi| > 37^\circ$

	Hard Limit and Actual Stratux	Hard Limit and Improved Stratux	Soft Limits and Actual Stratux	Soft Limits and Improved Stratux
Probability of Correct Detection	0.6329	0.5696	0.9494	0.7848
95% CI of Probability	0.5169 – 0.7386	0.4533 – 0.6806	0.8754 – 0.9860	0.6780 – 0.8694

In chapter 3 and chapter 4 we used the Private Pilot maneuver limit of 45° as our hazardous roll angle limit. In this section we varied the limit based on the data available in the test flights. The definition of the hazardous roll angle limit can vary for various reasons, including the phase of flight, height above the ground, or pilot certification level. Since Table 13 and Table 14 do not conclusively indicate the impact of the improved Stratux and soft limit on the accuracy of the Stratux, we find the correct detection probabilities by varying the magnitude of the roll angle limits. That is, we find: $p(|\phi_{Stratux}| > |\phi_{limit}| \mid |\phi_{G1000}| > |\phi_{limit}|)$, where ϕ_{limit} varies from $|20^\circ|$ to $|48^\circ|$ in the testing data set (5 flights) and $|20^\circ|$ to $|59^\circ|$ in the training data set (24 flights).

In Figure 29 and Figure 30, the cyan and the magenta plot lines are the detection probabilities when we use the soft limits for the Stratux. The magenta line also indicates the probabilities for the improved Stratux roll angles similar to the red line, which indicates the improved Stratux roll

angles without the soft limits. The blue line is the actual Stratux roll angle detection probabilities without the soft limits. The improved Stratux roll angles reduce the number of missed detections, but also increase the number of false alarms and do not improve upon the overall correct detection. Furthermore, at high magnitude angles the Stratux roll angles are highly erroneous and the models we created using the training data do not correct for the errors in the test data.

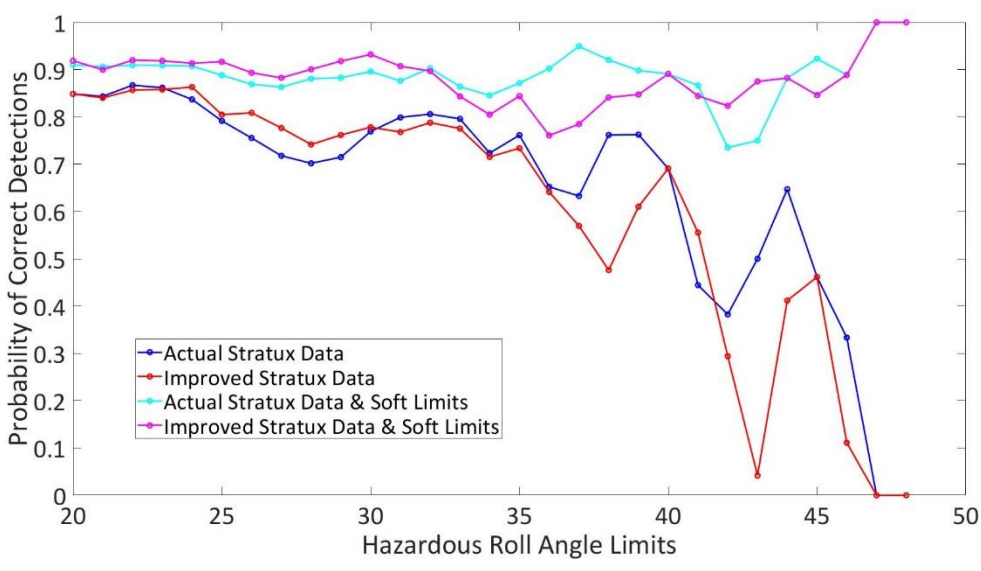


Figure 29: Correct Detection probabilities for varying roll angles for roll data in test flights. Model improved Stratux does not increase correct detections and do not perform well on test data.

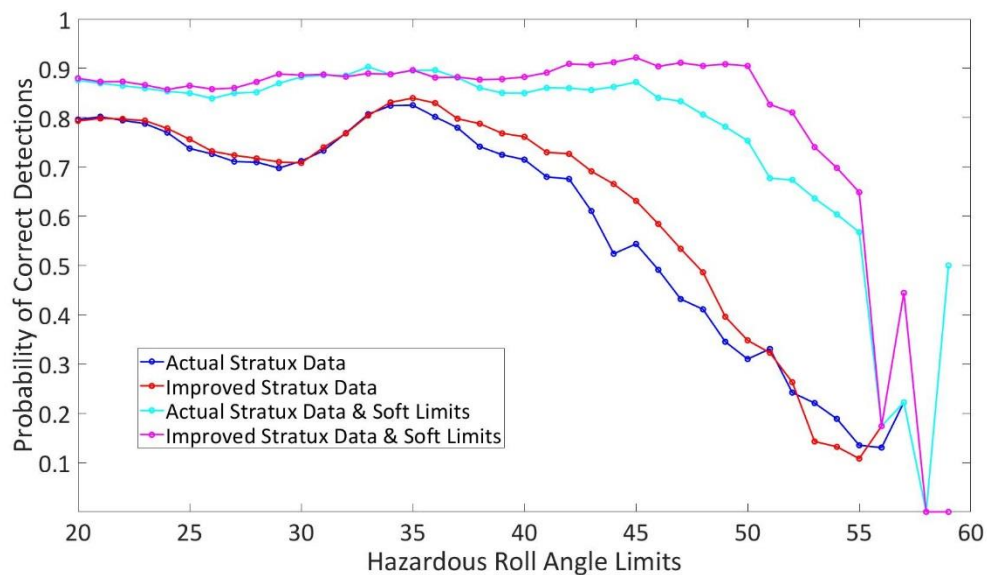


Figure 30: Correct Detection probabilities for varying roll angles for roll data in training flights. Modelled Stratux roll angle only marginally improve the detection and is specific to training data.

When using hard limits, the correct detection accuracy of the Stratux roll angles drop below 60% after the 40° limit angle. That is, for all hard limits below 40°, the actual Stratux data correctly detects angles beyond the limits with at least 60% accuracy.

As shown in Figure 29 and Figure 30, applying the soft limits always improve the detection of the roll angles higher in magnitude than the defined limit. The soft limits we developed from the training set ensure that the correct detection probability of the actual Stratux roll angles in the test data set remain above 70% for all roll angle limits ranging from $|20^\circ|$ to $|48^\circ|$. Using the soft limits in the training data, the probability of the actual Stratux roll angles correctly detecting angles higher in magnitude than the defined limit is above 80% for angles ranging from $|20^\circ|$ to $|48^\circ|$. In the training set, the probability of correct detection when using soft limits remains above 60% till $|54^\circ|$.

5.2 Detection of Risk Categories when using Soft Limits

Since the soft limits helped improve the detection of roll angles beyond a hazardous roll angle limit, in this section we test the impact of soft limits on risk category detection. Similar to section 4.4, we compare the risk categories from the Stratux and the G1000 roll angle data for the 5 test flights. We used the hazardous roll angle limit to define the risk levels (RL) and risk categories (RC) in section 4.1 and section 4.2. However, the soft limits for a given hard limit have two inner soft limits and two outer soft limits. We find the risk categories for the inner and outer soft limits separately.

For the test data of 5 flights, we redefined our hazardous roll angle limit to a hard value of $|19^\circ|$ in section 0. Since the soft limits for the positive and negative roll angles can be different, we use the absolute value of the mean of the limits. For example, the positive and negative inner soft limits for $|19^\circ|$ are 18.25° and -18.11° respectively, and we use $|18.18^\circ|$ as the inner soft limit for the risk level and risk category computations. Similarly, the outer soft limit is $|19.83^\circ|$.

Table 15, Table 16, and Table 17 show the conditional probabilities of the Stratux risk categories when using the hard limit of $|19^\circ|$, the inner soft limit, and outer soft limit respectively.

Table 15: Conditional Probabilities of the Stratux RC matching the G1000 RC for RL derived from equation 12 for a hard limit of $|19^\circ|$ on the test data.

		G1000			
		No Risk	Minor Risk	Moderate Risk	High Risk
Stratux	No Risk	0.9964	0.1541	0.0207	0.0036
	Minor Risk	0.0032	0.7670	0.2228	0.1950
	Moderate Risk	0.0004	0.0502	0.7047	0.0106
	High Risk	0	0.0287	0.0518	0.7908

Table 16: Conditional Probabilities of the Stratux RC matching the G1000 RC for RL derived from equation 12 for the inner soft limit of $|18.18^\circ|$ on the test data.

		G1000			
		No Risk	Minor Risk	Moderate Risk	High Risk
Stratux	No Risk	0.9970	0.1431	0.0315	0.0036
	Minor Risk	0.0027	0.8026	0.2087	0.0742
	Moderate Risk	0.0003	0.0477	0.6693	0.0106
	High Risk	0	0.0066	0.0906	0.9117

Table 17: Conditional Probabilities of the Stratux RC matching the G1000 RC for RL derived from equation 12 for the outer soft limit of $|19.83^\circ|$ on the test data.

		G1000			
		No Risk	Minor Risk	Moderate Risk	High Risk
Stratux	No Risk	0.9969	0.1660	0	0.0037
	Minor Risk	0.0026	0.7602	0.3600	0.1679
	Moderate Risk	0.0005	0.0574	0.5900	0
	High Risk	0	0.0164	0.0500	0.8284

The diagonal elements of the tables above give the conditional probability of the Stratux risk category exactly matching that of the G1000. As discussed in Section 4.4, ideally all the diagonal elements should be one and the sum of the elements should be four. Therefore, while comparing risk category probability tables, the one with the sum of diagonal elements closest to four has the highest accuracy of exact risk category detections. The elements above the diagonal provide the conditional probabilities for partial detection or complete missed detections. The elements below the diagonal provide the conditional probabilities of partial false alarms (i.e., a risk category higher than the one identified by the G1000) or complete false alarms. Ideally, all the elements above and below the diagonal, as well as their respective sums should be zero. Therefore, while comparing risk category probability tables, the table having the sum of elements below the diagonal closest to zero has the lowest overall missed detection probability, and the table having the sum of elements above the diagonal closest to zero has the lowest overall false alarm probability.

The information in Table 18 shows that using the inner soft limits increases risk category detections with a slight increase in probability of false alarms.

Table 18: Sum of the diagonal elements, the elements below the diagonal and the elements above the diagonal for Table 15, Table 16 and Table 17

	Hard limit of 19° 	Inner soft limit of 18.18° 	Outer soft limit of 19.83°
Sum of the diagonal elements	3.2589	3.3806	3.1755
Sum of the elements below the diagonal	0.1343	0.1479	0.1269
Sum of the elements above the diagonal	0.6068	0.4717	0.6979

Table 19 is similar to Table 18 except that we use equation (13) to find the risk levels and risk categories. APPENDIX C contains the three conditional probability tables when using equation (13). The data in Table 19 show that using the inner soft limits increases the probability of the Stratux in detecting risk categories, more closely matching that of the G1000. Therefore, irrespective of the risk level function we use, using inner soft limits to define the risk levels and risk categories improves the risk category detection of the Stratux.

Table 19: Sum of the diagonal elements, the elements below the diagonal and the elements above the diagonal of conditional probability tables when we use equation (13).

	Hard limit of 19° 	Inner soft limit of 18.18° 	Outer soft limit of 19.83°
Sum of the diagonal elements	2.8090	3.0035	2.8027
Sum of the elements below the diagonal	0.3198	0.2641	0.2854
Sum of the elements above the diagonal	0.8712	0.7324	0.9119

6. CONCLUSION AND FUTURE WORK

Using our Stratux device, we collected flight data via an android application. Compared to the G1000, the Stratux data missed 48% of the roll angles greater than 45° in our training set. Previous studies in automobile traffic information systems suggest that an accuracy level of 40% is not accurate enough to support user acceptance, but that 60% likely is [Fox, 1998]. Therefore, we developed two methods to increase the detection probability of angles beyond a hazardous roll angle limit when using the Stratux: (1) Use piecewise-discontinuous models to improve the Stratux roll angles and match that of the G1000, and (2) change the hazardous roll angle limit to soft limits for the Stratux. Piecewise-discontinuous models of the Stratux roll angle reduced the number of missed detections but increased the number of false alarms. Increasing false alarms can lead to decrease in user trust [Cafarelli, 1998], and when we incorporated false alarms in correct detection probability (equation 10), we found that the models we used to improve the Stratux roll angles in this research did not increase the detection probability of the Stratux. However, using soft limits substantially increases the detection probability of the Stratux for any definition of hazardous roll angle limit.

To capture time and angle accuracy, we defined risk level (RL) and risk category (RC). We compared the RCs generated from the G1000 and the Stratux roll data for varying RL functions. The advantage of RC comparison over hazardous angle comparison is that the RC comparison provides partial failure information whereas the hazardous angle comparison is either a success or a failure. The RC detection probabilities of the Stratux vary when we use different methods of computing the RLs. However, when using mapping functions to define the RLs, the resulting RC detection probabilities of the Stratux did not change for two different functions. We tested the

impact of using soft limits to define RL and RC. Inner soft limits (lower magnitude limit) of the Stratux helped increase the RC detection probabilities irrespective of the method we used to compute the RLs.

In our research, we used the Private Pilots' rolling maneuver limit of 45° (in training set). The FAA's GA Aviation Safety Information Analysis and Sharing (ASIAS) program can help in providing data to better determine the roll angle limit for safe operations.

We investigated a hazardous state based on a single flight parameter, but many aircraft hazardous states are complex and depend on multiple dependent variables. For example, the stalling speed of an aircraft increases with the increase in roll angle. We will need to investigate the methods discussed in this research when applied to more than one dependent variable defining a hazardous state.

The data collected in this research is from a single Stratux. To validate the methods and results we present in this research, we will need to apply the methods to additional low-cost AHRS devices. Additionally, one can find the optimum models for the Stratux roll angles, or the ideal risk level mapping function for roll angle and time.

APPENDIX A: LIST OF IMU BREAK-OUT BOARDS AND IMU SENSORS AVAILABLE AS OF SEPTEMBER 2017

Table 20: List of Hobbyist IMU breakout boards with 6 or more Degrees of Freedom (DOF)

Name	Price	Links [Accessed September 2017]
6 DOF Gyro, Accelerometer IMU - MPU6050	\$9.90	http://www.robotshop.com/en/6-dof-gyro-accelerometer-imu-mpu6050.html
6 Degrees of Freedom $\pm 2000^\circ/\text{sec}$ $\pm 16\text{g}$ IMU - ITG3200/ADXL345	\$31.96	http://www.robotshop.com/en/6-degrees-freedom-imu.html
MPU6050 6 DOF Gyro Accelerometer IMU	\$7.45	http://www.robotshop.com/en/mpu6050-6-dof-gyro-accelerometer-imu.html
6 DoF Accelerometer, Gyro Breakout Board - LSM6DS3	\$18.95	http://www.robotshop.com/en/6-dof-accelerometer-gyro-breakout-board--lsm6ds3.html
MPU-6050 6 DOF Gyro Accelerometer IMU	\$7.67	http://www.robotshop.com/en/mpu-6050-6-dof-gyro-accelerometer-imu.html
6 DOF Gyro, Accelerometer IMU Breakout Board - MPU6050	\$27.82	http://www.robotshop.com/en/6-dof-gyro-accelerometer-imu-breakout-board-mpu6050.html
PhidgetSpatial Precision 3/3/3 High Res 3 Axis Compass/Gyroscope/Accelerometer	\$140.00	http://www.robotshop.com/en/phidgetspatial-precision-3-33-high-res-3-axis-compassgyroscopeaccelerometer.html
RoBoard RM-G146 9-Axis Accelerometer, Gyro and Compass	\$81.13	http://www.robotshop.com/en/roboard-rm-g146-9-axis-accelerometer-gyro-compass.html
FLORA Adafruit LSM9DS0 9DoF $\pm 2000^\circ/\text{sec}$ $\pm 16\text{g}$ IMU	\$17.96	http://www.robotshop.com/en/flora-adafruit-lsm9ds0-9dof-2000-sec-16g-imu.html
Adafruit LSM9DS0 9DoF $\pm 2000^\circ/\text{sec}$ $\pm 16\text{g}$ IMU	\$22.46	http://www.robotshop.com/en/adafruit-lsm9ds0-9dof-2000-sec-16g-imu.html
BNO055 9 DOF Absolute Orientation IMU Fusion Breakout Board	\$31.46	http://www.robotshop.com/en/bno055-9-dof-absolute-orientation-imu-fusion-breakout-board.html
9 Degrees of Freedom Block for Intel Edison	\$15.15	http://www.robotshop.com/en/9-degrees-freedom-block-intel-edison.html
9DoF AltIMU-10 Gyro/Accelerometer/Compass/Altimeter	\$20.95	http://www.robotshop.com/en/10dof-altimu-10-gyro-accelerometercompassaltimeter.html

Table 20: List of Hobbyist IMU breakout boards with 6 or more Degrees of Freedom (DOF)

Name	Price	Links [Accessed September 2017]
Grove - 9DoF $\pm 2000^\circ/\text{sec}$ $\pm 16\text{g}$ IMU	\$12. 38	http://www.robotshop.com/en/grove-9dof-2000-sec-16g-imu.html
LSM9DS1 9DoF $\pm 2000^\circ/\text{sec}$ $\pm 16\text{g}$ IMU	\$23. 70	http://www.robotshop.com/en/lsm9ds1-9dof-2000-sec-16g-imu.html
MinIMU-9 v5 Gyro, Accelerometer and Compass (LSM6DS33 and LIS3MDL Carrier)	\$11. 95	http://www.robotshop.com/en/minimu-9-v5-gyro-accelerometer-compass-lsm6ds33-and-lis3mdl-carrier.html
Ocotpus 9DoF $\pm 2000^\circ/\text{sec}$ $\pm 16\text{g}$ IMU Brick	\$19. 76	http://www.robotshop.com/en/ocotpus-9dof-2000-sec-16g-imu-brick.html
IMU Breakout Board - MPU-9250	\$14. 20	http://www.robotshop.com/en/imu-breakout-board-mpu-9250.html
9 Degrees of Freedom - Razor M0 IMU	\$47. 45	http://www.robotshop.com/en/9-degrees-of-freedom-razor-m0-imu.html
Variense Compact IMU 9-Axis	\$58. 20	http://www.robotshop.com/en/variense-compact-imu-9-axis-vmu931.html
UM7-LT Orientation Sensor (AHRS)	\$134. .35	http://www.robotshop.com/en/um7-lt-orientation-sensor.html
Adafruit Precision NXP 9-DOF Breakout Board - FXOS8700 + FXAS21002	\$13. 46	http://www.robotshop.com/en/adafruit-precision-nxp-9-dof-breakout-board-fxos8700-fxas21002.html
LSM9DS1 9DoF $\pm 2000^\circ/\text{sec}$ $\pm 16\text{g}$ IMU Breakout Board	\$13. 46	http://www.robotshop.com/en/lsm9ds1-9dof-2000-sec-16g-imu-breakout-board.html
IMU 10 DOF $\pm 16\text{g}$ 3 Axis Accelerometer $\pm 2000^\circ/\text{s}$ Gyro/Magnetometer/Barometer	\$37. 34	http://www.robotshop.com/en/imu-10-dof-16g-3-axis-accelerometer-2000--s-gyromagnetometerbarometer.html
Xadow IMU 10 DOF	\$16. 39	http://www.robotshop.com/en/xadow-imu-10-dof.html
AltIMU-10 v5 Gyro, Accelerometer, Compass and Altimeter (LSM6DS33, LIS3MDL, and LPS25H Carrier)	\$17. 25	http://www.robotshop.com/en/altimu-10-v5-gyro-accelerometer-compass-altimeter-lsm6ds33-lis3mdl-and-lps25h-carrier.html
Grove IMU 10DOF v2.0	\$16. 39	http://www.robotshop.com/en/grove-imu-10dof-v20.html

Table 20: List of Hobbyist IMU breakout boards with 6 or more Degrees of Freedom (DOF)

Name	Price	Links [Accessed September 2017]
IMU 10 DOF $\pm 16g$ 3 Axis Accelerometer ± 2000 $^{\circ}/s$ Gyro/Magnetometer/Barometer	\$15. 03	http://www.robotshop.com/en/imu-10-dof-16g-3-axis-accelerometer-2000--s-gyromagnetometerbarometer-c.html

Table 21: List of IMU Sensors, the manufacturers, unit price and types of sensors, arranged in increasing order of unit price.

Manufacturer Part Number	Manufacturer	Unit Price (USD)	Types of Sensors in the IMU
LSM6DS3TR	STMicroelectronics	1.40928	Accelerometer, Gyroscope, 3 Axis
LSM330TR	STMicroelectronics	1.4497	Accelerometer, Gyroscope, 3 Axis
LSM6DS33TR	STMicroelectronics	1.46433	Accelerometer, Gyroscope, 3 Axis
LSM6DS0TR	STMicroelectronics	1.5295	Accelerometer, Gyroscope, 3 Axis
LSM6DS3HTR	STMicroelectronics	1.86496	Accelerometer, Gyroscope, Temperature, 6 Axis
LSM6DSMTR	STMicroelectronics	1.92	Accelerometer, Gyroscope, 3 Axis
LSM6DSLTR	STMicroelectronics	1.92	Accelerometer, Gyroscope, 3 Axis
LSM6DSLUSTR	STMicroelectronics	1.92	Not available
BMI160	Bosch Sensortec	1.944	Accelerometer, Gyroscope, 3 Axis
ICM-20602	TDK InvenSense	2.0655	Accelerometer, Gyroscope, Temperature, 6 Axis
ICM-20689	TDK InvenSense	2.53125	Accelerometer, Gyroscope, Temperature, 6 Axis
LSM330DLCTR	STMicroelectronics	2.54695	Accelerometer, Gyroscope, 3 Axis
BMI055	Bosch Sensortec	2.5785	Accelerometer, Gyroscope, 3 Axis
ICM-20648	TDK InvenSense	2.7945	Accelerometer, Gyroscope, Temperature, 6 Axis

Table 21: List of IMU Sensors, the manufacturers, unit price and types of sensors, arranged in increasing order of unit price.

Manufacturer Part Number	Manufacturer	Unit Price (USD)	Types of Sensors in the IMU
LSM330TR	STMicroelectronics	2.98	Accelerometer, Gyroscope, 3 Axis
LSM330TR	STMicroelectronics	Not available	Accelerometer, Gyroscope, 3 Axis
LSM6DS3TR	STMicroelectronics	3.01	Accelerometer, Gyroscope, 3 Axis
LSM6DS3TR	STMicroelectronics	Not available	Accelerometer, Gyroscope, 3 Axis
LSM6DS33TR	STMicroelectronics	3.01	Accelerometer, Gyroscope, 3 Axis
LSM6DS33TR	STMicroelectronics	Not available	Accelerometer, Gyroscope, 3 Axis
LSM9DS1TR	STMicroelectronics	3.12018	Accelerometer, Gyroscope, Magnetometer, 3 Axis
LSM6DS0TR	STMicroelectronics	3.14	Accelerometer, Gyroscope, 3 Axis
LSM6DS0TR	STMicroelectronics	Not available	Accelerometer, Gyroscope, 3 Axis
BMX055	Bosch Sensortec	3.3915	Accelerometer, Gyroscope, Magnetometer, 3 Axis
ICM-20948	TDK InvenSense	3.6841	Accelerometer, Gyroscope, Magnetometer, 3 Axis
ICM-30630	TDK InvenSense	3.76656	Accelerometer, Gyroscope, 3 Axis
LSM6DS3HTR	STMicroelectronics	3.98	Accelerometer, Gyroscope, Temperature, 6 Axis
LSM6DS3HTR	STMicroelectronics	Not available	Accelerometer, Gyroscope, Temperature, 6 Axis
LSM6DSMTR	STMicroelectronics	4.09	Accelerometer, Gyroscope, 3 Axis
LSM6DSMTR	STMicroelectronics	Not available	Accelerometer, Gyroscope, 3 Axis
LSM6DSLTR	STMicroelectronics	4.09	Accelerometer, Gyroscope, 3 Axis

Table 21: List of IMU Sensors, the manufacturers, unit price and types of sensors, arranged in increasing order of unit price.

Manufacturer Part Number	Manufacturer	Unit Price (USD)	Types of Sensors in the IMU
LSM6DSLTR	STMicroelectronics	Not available	Accelerometer, Gyroscope, 3 Axis
FIS1100	Fairchild/ON Semiconductor	4.13875	Accelerometer, Gyroscope, 3 Axis
MPU-9250	TDK InvenSense	4.5087	Accelerometer, Gyroscope, Magnetometer, 3 Axis
BHI160	Bosch Sensortec	4.655	Accelerometer, Gyroscope, 3 Axis
LSM330DLCTR	STMicroelectronics	5.23	Accelerometer, Gyroscope, 3 Axis
LSM330DLCTR	STMicroelectronics	Not available	Accelerometer, Gyroscope, 3 Axis
BNO055	Bosch Sensortec	5.29375	Accelerometer, Gyroscope, Magnetometer, 3 Axis
BMI160	Bosch Sensortec	5.39	Accelerometer, Gyroscope, 3 Axis
BMI160	Bosch Sensortec	Not available	Accelerometer, Gyroscope, 3 Axis
BMF055	Bosch Sensortec	5.6925	Accelerometer, Gyroscope, Magnetometer, 3 Axis
ICM-20602	TDK InvenSense	5.72	Accelerometer, Gyroscope, Temperature, 6 Axis
ICM-20602	TDK InvenSense	Not available	Accelerometer, Gyroscope, Temperature, 6 Axis
LSM9DS1TR	STMicroelectronics	6.4	Accelerometer, Gyroscope, Magnetometer, 3 Axis
LSM9DS1TR	STMicroelectronics	Not available	Accelerometer, Gyroscope, Magnetometer, 3 Axis
ICM-20689	TDK InvenSense	7.01	Accelerometer, Gyroscope, Temperature, 6 Axis
ICM-20689	TDK InvenSense	Not available	Accelerometer, Gyroscope, Temperature, 6 Axis
BMI055	Bosch Sensortec	7.14	Accelerometer, Gyroscope, 3 Axis

Table 21: List of IMU Sensors, the manufacturers, unit price and types of sensors, arranged in increasing order of unit price.

Manufacturer Part Number	Manufacturer	Unit Price (USD)	Types of Sensors in the IMU
BMI055	Bosch Sensortec	Not available	Accelerometer, Gyroscope, 3 Axis
ICM-20648	TDK InvenSense	7.74	Accelerometer, Gyroscope, Temperature, 6 Axis
ICM-20648	TDK InvenSense	Not available	Accelerometer, Gyroscope, Temperature, 6 Axis
BMX055	Bosch Sensortec	7.99	Accelerometer, Gyroscope, Magnetometer, 3 Axis
BMX055	Bosch Sensortec	Not available	Accelerometer, Gyroscope, Magnetometer, 3 Axis
ICM-20948	TDK InvenSense	8.68	Accelerometer, Gyroscope, Magnetometer, 3 Axis
ICM-20948	TDK InvenSense	Not available	Accelerometer, Gyroscope, Magnetometer, 3 Axis
ICM-30630	TDK InvenSense	8.88	Accelerometer, Gyroscope, 3 Axis
ICM-30630	TDK InvenSense	Not available	Accelerometer, Gyroscope, 3 Axis
FIS1100	Fairchild/ON Semiconductor	9.44	Accelerometer, Gyroscope, 3 Axis
FIS1100	Fairchild/ON Semiconductor	Not available	Accelerometer, Gyroscope, 3 Axis
MPU-9250	TDK InvenSense	10.63	Accelerometer, Gyroscope, Magnetometer, 3 Axis
MPU-9250	TDK InvenSense	Not available	Accelerometer, Gyroscope, Magnetometer, 3 Axis
BNO055	Bosch Sensortec	12.07	Accelerometer, Gyroscope, Magnetometer, 3 Axis
BNO055	Bosch Sensortec	Not available	Accelerometer, Gyroscope, Magnetometer, 3 Axis
BHI160	Bosch Sensortec	12.4	Accelerometer, Gyroscope, 3 Axis
BHI160	Bosch Sensortec	Not available	Accelerometer, Gyroscope, 3 Axis

Table 21: List of IMU Sensors, the manufacturers, unit price and types of sensors, arranged in increasing order of unit price.

Manufacturer Part Number	Manufacturer	Unit Price (USD)	Types of Sensors in the IMU
BMF055	Bosch Sensortec	12.98	Accelerometer, Gyroscope, Magnetometer, 3 Axis
BMF055	Bosch Sensortec	Not available	Accelerometer, Gyroscope, Magnetometer, 3 Axis
MM7150-AB0	Microchip Technology	24.73	Accelerometer, Gyroscope, Magnetometer, 3 Axis
MM7150-AB1	Microchip Technology	24.73	Accelerometer, Gyroscope, Magnetometer, 3 Axis
MM7150I-AB1	Microchip Technology	30.91	Accelerometer, Gyroscope, Magnetometer, 3 Axis
SCC2230-E02-05	Murata Electronics North America	62.925	Accelerometer, Gyroscope, 3 Axis
SCC2230-D08-05	Murata Electronics North America	62.925	Accelerometer, Gyroscope, 3 Axis
SCC2130-D08-05	Murata Electronics North America	62.925	Accelerometer, Gyroscope, 3 Axis
SCC1300-D02-6	Murata Electronics North America	81.8615	Accelerometer, Gyroscope, 3 Axis
SCC1300-D04-6	Murata Electronics North America	81.8615	Accelerometer, Gyroscope, 3 Axis
SCC1300-D02-05	Murata Electronics North America	89.2476	Accelerometer, Gyroscope, 3 Axis
SCC1300-D04-05	Murata Electronics North America	89.2476	Accelerometer, Gyroscope, 3 Axis
SCC2230-E02-05	Murata Electronics North America	92.29	Accelerometer, Gyroscope, 3 Axis
SCC2230-E02-05	Murata Electronics North America	Not available	Accelerometer, Gyroscope, 3 Axis
SCC2230-D08-05	Murata Electronics North America	92.29	Accelerometer, Gyroscope, 3 Axis
SCC2230-D08-05	Murata Electronics North America	Not available	Accelerometer, Gyroscope, 3 Axis
SCC2130-D08-05	Murata Electronics North America	92.29	Accelerometer, Gyroscope, 3 Axis

Table 21: List of IMU Sensors, the manufacturers, unit price and types of sensors, arranged in increasing order of unit price.

Manufacturer Part Number	Manufacturer	Unit Price (USD)	Types of Sensors in the IMU
SCC2130-D08-05	Murata Electronics North America	Not available	Accelerometer, Gyroscope, 3 Axis
MTI-1-8A7G6T	XSens Technologies BV	185.6	Accelerometer, Gyroscope, Magnetometer, 3 Axis
MTI-2-8A7G6T	XSens Technologies BV	288	Accelerometer, Gyroscope, Magnetometer, 3 Axis
MTI-3-8A7G6T	XSens Technologies BV	369.92	Accelerometer, Gyroscope, Magnetometer, 3 Axis
HG1120AA50	Honeywell Microelectronics & Precision Sensors	1062.67	Accelerometer, Gyroscope, Magnetometer, 3 Axis
MTI-20-2A5G4	XSens Technologies BV	1298.08	Accelerometer, Gyroscope, Magnetometer, 3 Axis
HG1120BA50	Honeywell Microelectronics & Precision Sensors	1328.67	Accelerometer, Gyroscope, Magnetometer, 3 Axis
MTI-30-2A5G4	XSens Technologies BV	1518.4	Accelerometer, Gyroscope, Magnetometer, 3 Axis
HG1120CA50	Honeywell Microelectronics & Precision Sensors	1594.67	Accelerometer, Gyroscope, Magnetometer, 3 Axis
S4E5A0A0A111 J00	Epson Electronics America Inc-Semiconductor Div	2304	Accelerometer, Gyroscope, 3 Axis
HG4930AA51	Honeywell Microelectronics & Precision Sensors	6998.75	Accelerometer, Gyroscope, 3 Axis
HG4930BA51	Honeywell Microelectronics & Precision Sensors	8498.75	Accelerometer, Gyroscope, 3 Axis
HG4930CA51	Honeywell Microelectronics & Precision Sensors	9998.75	Accelerometer, Gyroscope, 3 Axis

APPENDIX B. LIST OF STRATUX VARIABLES RECORDED

This section describes the variables accessed through <http://192.168.10.1/getSituation> for the Stratux.

1. ***GPSTimeSinceMidnightUTC***

The time from midnight UTC (Zulu) in seconds.

2. ***GPSLatitude***

Latitude of position. South is negative.

3. ***GPSLongitude***

Longitude of position. West is negative.

4. ***GPSHeightAboveEllipsoid***

GPS height (in feet) above WGS84 ellipsoid.

5. ***GPSAltitudeMSL***

GPS height (in feet) above Mean Sea Level.

6. ***GPSGeoidSep***

Difference between GPSHeightAboveEllipsoid and GPSAltitudeMSL (HAE – AltMSL).

7. ***GPSPositionSampleRate***

The variable provides the calculated mean sample rate of GPS positions and other GPS data.

8. ***GPSSatellitesTracked***

Number of satellites from which almanac data is received.

9. ***GPSSatellites***

Number of Satellites used in solution. Increases by 1 in GPSFixQuality is 2. The value is zero if no GPS.

10. ***GPSSatellitesSeen***

GPS Satellites from which signal is received.

11. ***GPSTurnRate***

The variable provides the calculated turn rate in deg/sec. The turn rate is calculated as the slope of the linear regression of GPS heading.

12. ***GPSGroundSpeed***

Groundspeed from GPS converted to knots.

13. ***GPSTrueCourse***

True flight course. Set to -999.9 if ground speed < 3knots.

14. ***GPSVerticalSpeed***

GPS vertical speed in ft/s. Climbing is positive vertical speed.

15. ***GPSTLastValidNMEAMessageTime***

The last time a valid NMEA message was received. Set to Stratux Clock Time.

16. ***GPSTLastGPSTimeStratuxTime***

Previous Stratux Clock time at which all GPS time was recorded.

17. ***GPSTLastGroundTrackTime***

Stratux clock time after groundspeed and course has been computed.

18. ***GPSTLastFixLocalTime***

Stratux clock time recorded once fix and altitude is recorded and before ground speed and track is determined.

19. ***GPSTime***

GPS time as is. Raw GPS time value. Date in format: YYYY-MM-DD and time in format: 'hours: minutes: seconds'. [Note: Stratux Clock is set to GPS time when update required.]

20. ***GPSTFixQuality***

Determines how the position fix of GPS has been computed. The value is dependent on NMEA information.

Table 22: Description of ‘GPSFixQuality’ values.

GPSFixQuality Value	Description
2	2D or 3D differential GPS used in computing fix
1	2D or 3D GPS used in computing fix
6	Dead reckoning or a combination of 1 GPS and dead reckoning used
0	No fix or no GPS

21. *GPSVerticalAccuracy*

- If UBX (i.e. GPSTimeValidNMEAMessage first component reads PUBX) Vertical accuracy of GPS position fix reported to 1-sigma variation. It is twice the GPSHorizontalAccuracy.
- If GPSTimeValidNMEAMessage first component reads GNGSA or GPGSA, then vertical accuracy of GPS position fix is $5 * (\text{Vertical Dilution of Precision (vdop)})$.
- When no GPS, the value is 999999

22. *GPSHorizontalAccuracy*

- If UBX (i.e. GPSTimeValidNMEAMessage first component reads PUBX) Horizontal accuracy of GPS position fix reported with 1-sigma variation.
- If GPSTimeValidNMEAMessage first component reads GNGSA or GPGSA, then horizontal accuracy is:
 - if GPSFixQuality is 2: $4 * (\text{Horizontal Dilution of Precision (hdop)})$
 - else: $8 * (\text{Horizontal Dilution of Precision (hdop)})$
- When no GPS, the value is 999999.

23. *GPSNACp*

Horizontal accuracy of GPS position fix reported with 95% confidence (2-sigma) in variation (As per AC 20-165A).

Table 23: Horizontal positional accuracy corresponding to ‘GPSNACp’ values.

GPSNACp Value	Accuracy Range
11	Horizontal accuracy < 3m
10	3m < Horizontal Accuracy < 10m
9	10m < Horizontal Accuracy < 30m
8	30m < Horizontal accuracy < 92.6m
7	92.6m < Horizontal accuracy < 185.2m
6	185.2m < Horizontal accuracy < 55.6m
0	No GPS

24. *GPSTLastValidNMEAMessage*

Last NMEA message processed.

25. *BaroTemperature*

Temperature from BMP 280 in degree centigrade. Note that, it provides temperature of immediate surrounding and in this case, the temperature within the Stratux box. Should not be used as OAT.

26. *BaroPressureAltitude*

Provides the ISA pressure altitude based on the local pressure sensed, since no correction applied.

Used in computing Baro Vertical speed.

27. *BaroVerticalSpeed*

Vertical speed computed based on Barometric altitude. ‘dt’ is the delta time and set to 0.1.

Parameter ‘u’ is used to set 5 sec decay time for rate of climb.

$$BaroVSpd = u * BaroVSpd_{prev} + (1 - u) * (alt - alt_{prev}) * \frac{60}{dt}$$

If sensor value not available, BaroVerticalSpeed is set to 99999.

28. *BaroLastMeasurementTime*

Set to Stratux clock time

29. *AHRSPitch*

Euler Pitch angle computed based on Kalman Filter fusion of IMU (accelerometer & gyroscope) and GPS computed pitch. Up is positive.

30. *AHRRoll*

Euler Roll angle computed based on Kalman Filter fusion of IMU (accelerometer & gyroscope) and GPS computed roll. Right turn is positive.

31. *AHRSGyroHeading*

Initialized to GPS True Course.

Euler Heading angle computed based on Kalman Filter fusion of IMU (accelerometer & gyroscope) and GPS computed true course.

32. *AHRSMagHeading*

Euler Heading angle computed based on magnetometer reading. Even though this computation is performed, it is currently not in use since magnetometer calibration has not been implemented.

Contains 3276.7 as a dummy value.

33. *AHRSSlipSkid*

Slip and Skid angle computed in degrees from Kalman Filter of IMU and GPS sensors. Right turn is positive.

34. *AHRSTurnRate*

Turn Rate computed in degrees per second from Kalman Filter fusion of GPS an IMU sensor data.

Right turn is positive.

35. *AHRSGLoad*

Provides the load factor in 'g's. Computed using IMU sensors.

36. *AHRSGLoadMin*

The minimum G-load experienced till the time of computation. If the next G-load is lower than existing GloadMin, GloadMin is updated.

37. *AHRSGLoadMax*

The maximum Gload experienced till the time of computation. If the next G-load is greater than existing GloadMax, GloadMax is updated.

38. *AHRSLastAttitudeTime*

Set to Stratux clock when either GPS is valid or when GPS calculated altitude is available.

39. *AHRSStatus*

This variable is a numerical representation of the state of the Stratux components contributing to AHRS computation and debugging.

Table 24: Description of State Identification Numbers in the Stratux software.

State Identification Number	Description
1	GPS ground track is valid. The aircraft is moving.
2	IMU is enabled and working
4	Pressure sensor is enabled and working
8	AHRS Calibration in progress
16	Logging to csv

The AHRSStatus is a sum of one or more of the State identification numbers in the table above.

APPENDIX C: THE CONDITIONAL PROBABILITY TABLES OF THE STRATUX RISK CATEGORIES WHEN USING EQUATION(13 TO GENERATE THE RISK LEVELS

Table 25: Conditional Probabilities of the Stratux RC matching the G1000 RC for RL derived from equation (13 for a hard limit of $|19^\circ|$ on the test data.

		G1000			
		No Risk	Minor Risk	Moderate Risk	High Risk
Stratux	No Risk	0.9974	0.4922	0.1000	0.0056
	Minor Risk	0.0019	0.3281	0.2188	0.0038
	Moderate Risk	0.0007	0.1719	0.5438	0.0508
	High Risk	0	0.0078	0.1375	0.9397

Table 26: Conditional Probabilities of the Stratux RC matching the G1000 RC for RL derived from equation (13 for the inner soft limit of $|18.18^\circ|$ on the test data.

		G1000			
		No Risk	Minor Risk	Moderate Risk	High Risk
Stratux	No Risk	0.9959	0.3409	0.1026	0.0053
	Minor Risk	0.0028	0.5170	0.2205	0.0088
	Moderate Risk	0.0013	0.1364	0.5590	0.0544
	High Risk	0	0.0057	0.1179	0.9316

Table 27: Conditional Probabilities of the Stratux RC matching the G1000 RC for RL derived from equation 12 for the outer soft limit of $|19.83^\circ|$ on the test data.

		G1000			
		No Risk	Minor Risk	Moderate Risk	High Risk
Stratux	No Risk	0.9971	0.4643	0.1688	0.0020
	Minor Risk	0.0024	0.3571	0.1753	0.0020
	Moderate Risk	0.0005	0.1786	0.5519	0.0994
	High Risk	0	0	0.1039	0.8966

REFERENCES

- AC No: 120-76C (2014). Advisory Circular (AC No: 120-76C): Guidelines for the Certification, Airworthiness, and Operational Use of Electronic Flight Bags, Federal Aviation Administration, May 2014.
- AC No: 120-82 (2004). Advisory Circular (AC No: 120-82): Flight Operational Quality Assurance, Federal Aviation Administration, April 2004
- AC No: 20-181 (2014). Advisory Circular (AC No: 20-181): Airworthiness Approval of Attitude Heading Reference System (AHRS) Equipment ,April 2014.
- AC No: 91.21-1D (2017). Advisory Circular (AC No: 91.21-1D): Use of Portable Electronic Devices Aboard Aircraft, Federal Aviation Administration, October 2017.
- ACS (2018). American Chemical Society (ACS), “Risk Rating and Assessment,” URL: <https://www.acs.org/content/acs/en/about/governance/committees/chemicalsafety/hazard-assessment/fundamentals/risk-assessment.html>. Accessed 06 November 2018.
- Albéri, M., Baldoncini, M., Bottardi, C., Chiarelli, E., Fiorentini, G., Giulia, K., Raptis, C., Realini, E., Reguzzoni, M., Rossi, L., Sampietro, D., Strati, V., and Mantovani, F. (2017). Accuracy of Flight Altitude Measured with Low-Cost GNSS, Radar and Barometer Sensors: Implications for Airborne Radiometric Surveys, Sensors 2017.
- Bonadonna, C., Brody, D., Lopez, A. (2015). Design of a Low-Cost General Aviation Flight Data Recording and Analysis System, 2015 IEEE Systems and Information Engineering Design Symposium, 2015.
- Cafarelli, A. D. (1998). Effect of False Alarm Rate on Pilot Use and Trust of Automation under Conditions of Simulated High Risk, MS Thesis, Aeronautics and Astronautics, Massachusetts Institute of Technology, September 1998.

- Cirrus POH (2003). Pilot's Operating Handbook and FAA Approved Flight Manual for Cirrus Design SR 20, 2003, Page: 2-10
- Clopper, J.C., Pearson, S. E. (1934). The Use of Confidence or Fiducial Limits Illustrated in the Case of the Binomial, *Biometrika*, Vol. 26, No. 4. (Dec., 1934), pp. 404-413.
- Darby, R. (2010). Safety in Numbers, Flight Safety Foundation, July 2010.
- Dejan (2018). How to Mechatronics: MEMS Accelerometer Gyroscope Magnetometer & Arduino: <https://howtomechatronics.com/how-it-works/electrical-engineering/mems-accelerometer-gyroscope-magnetometer-arduino/>. Accessed September, 2018.
- Fala, N., and Marais, K. (2016). Detecting Safety Events during Approach in General Aviation Operations, 16th AIAA Aviation Technology, Integration, and Operations Conference, 2016.
- Federal Aviation Administration (FAA) (2008). Plane Sense General Aviation Information (FAA-H-8083-19A), 2008
- Federal Aviation Administration (FAA) (2018). Fact Sheet – General Aviation Safety: https://www.faa.gov/news/fact_sheets/news_story.cfm?newsId=21274. Accessed September, 2018.
- Federal Aviation Administrator (FAA) (2018). Private Pilot- Airman Certification Standards, FAA, June 2018.
- Fox, E. H. F. (1998). The Effects of Age and ATTS Congestion Information Accuracy on User Trust and Compliance, Ph.D. Thesis, Department of Psychology, George Mason University, 1998..
- Garmin (2010). GRS 77/GMU 44 Installation Manual, Revision L, March 2010.
- Garmin (2015). Cirrus SR2x Integrated Avionics System Pilot's Guide, December 2015.

- General Aviation Manufacturer's Association (GAMA) (2017). 2017 Annual Report, 2017
- Goblet, V., Fala, N., and Marais, K. (2015). Identifying Phases of Flight in General Aviation Operations, 15th AIAA Aviation Technology, Integration, and Operations Conference, 2015.
- Groves, D. P. (2008). Principles of GNSS, Inertial, and Multisensor Integrated Navigation Systems, Artech House, 2008.
- Hunter, R. D. (2002). Risk Perception and Risk Tolerance in Aircraft Pilots, FAA Office of Aerospace Medicine, 2002.
- Hunter, R. D. (2006). Risk Perception Among General Aviation Pilots, The International Journal of Aviation Psychology, 16:2, 135-144, DOI: 10.1207/s15327108ijap1602_1
- International Civil Aviation Organization (ICAO) (2009). Tenth Session of the Statistics Division, 2009
- Jiao, Y., Sun, H., Wang, C., and Han, J. (2018). Research on Unstable Approach Detection of Civil Aviation Aircraft, 8th International Congress of Information and Communication Technology (ICICT-2018).
- Knecht, R. W. and Frazier, E. (2015). Pilots' Risk Perception and Risk Tolerance Using Graphical Risk-Proxy Gradients, Federal Aviation Administration, Office of Aerospace Medicine, Washington, DC 20591, May 2015.
- Krak, E. (2014). Goniometer software solution for testing of attitude indicators, , Bachelor's Diploma Thesis, Universitas Masarykiana, 2014, Brno
- Kuo, C. B., Guan, W., Chen, P. (2017). In Search of General Aviation Flight Data Monitoring: Lightweight Recording System, 17th AIAA Aviation Technology, Integration, and Operations Conference, 2017.

- KVH Industries (2014). White Paper: Guide to Comparing Gyro and IMU Technologies- Micro-Electro-Mechanical Systems and Fiber Optic Gyros, 2014.
- Lau, K. S. (2007). General Aviation Flight Data Monitoring, Fly with Intelligence – Best Practices to Improve the Safety and Efficiency of Flight Operations, CAPACG White Paper, March 2007.
- Madgwick, O. H. S. (2010). An efficient orientation filter for inertial and inertial/magnetic sensor arrays, 2010.
- Mahony, R., Euston, M., Kim, J., Coote, P., and Hamel, T. (2011). A non-linear observer for attitude estimation of a fixed-wing unmanned aerial vehicle without GPS measurements; Transactions of the Institute of Measurement and Control 33, 2011.
- Mahony, R., Hammel, T., and Pflimlin, M. J. (2008). Nonlinear Complementary Filters on the Special Orthogonal Group, IEEE Transactions on Automatic Control, 2008.
- Markley, L. F., and Mortari, D. (2000). Quaternion Attitude Estimation Using Vector Observations, Journal of the Astronautical Sciences, Vol. 48, No. 2/3, 2000, pp. 359–380
- National Transportation Safety Board (NTSB) (2018). National Transportation Safety Board Aviation Accident Factual Report, Accident Number: CEN17FA084, Oct 04, 2018.
- Neuhart, A. R., Gingras, R. D., Hultberg, S. R., Oltman, S. R., and Nathan W. Graybeal (2009). Flight Data Collection for General Aviation Aircraft Simulation Validation, AIAA Atmospheric Flight Mechanics Conference, 10 - 13 August 2009.
- NTSB (2016). National Transportation Safety Board: US Transportation Fatalities in 2016 – by Mode.

- PRIME Faraday Partnership (2002). An Introduction to MEMS; Prime Faraday Technology Watch – January, 2002, ISBN 1-84402-020-7, Wolfson School of Mechanical and Manufacturing Engineering.
- Puranik, G. T. and Mavris, N. D. (2018). Anomaly Detection in General-Aviation Operations Using Energy Metrics and Flight-Data Records, Journal of Aerospace Information Systems Vol. 15, No. 1, January 2018.
- Rao, A. H. and Marais, K. (2016). Comparing Hazardous States and Trigger Events in Fatal and Non-Fatal Helicopter Accidents, 16th AIAA Aviation Technology, Integration, and Operations Conference, 2016.
- RTCA DO-334 (2012). Standard: RTCA DO-334: Minimum Operational Performance Standards (Mops) For Strapdown Attitude And Heading Reference Systems (AHRS): <https://standards.globalspec.com/std/1538865/rtca-do-334>. Accessed September 2018.
- Sandman, M. P., Weinstein, D. N., and Miller, P. (1994). High Risk or Low: How Location on a "Risk Ladder" Affects Perceived Risk, Society for Risk Analysis, 1994.
- Stratux (2018). Stratux ADS-B: DIY/Low-cost portable ADS-B: <http://stratux.me/>. Accessed September 2018.
- Stratux App Integration (2018). Github: App Side Integration: <https://github.com/cyoung/stratux/blob/master/notes/app-vendor-integration.md>. Accessed September 2018.
- Townsend, K. (2018). Adafruit: Sensor Fusion Algorithms: <https://learn.adafruit.com/ahrs-for-adafruits-9-dof-10-dof-breakout/sensor-fusion-algorithms>. Accessed September 2018.

- Valasek, J., Harris, J., Pruchnicki, S., McCrink, M., Gregory, J., and Sizoo, G. D. (2017). Characterization of Derived Angle-of-Attack and Sideslip Angle Algorithms Using Monte Carlo and Piloted Simulation, AIAA Atmospheric Flight Mechanics Conference, 5-9 June 2017.
- Valenti, G. R., Dryanovski, I. and Xiao, J. (2015). Keeping a Good Attitude: A Quaternion-Based Orientation Filter for IMUs and MARGs, Sensors, 2015;
- Vectornav- Embedded Navigation Solutions (2018). VN-100: <https://www.vectornav.com/products/vn-100>. Accessed September 2018.
- Wabha, G. (1965). Problem 65-1: A Least Squares Estimate of Satellite Attitude, SIAM Review, Vol. 7, No. 3. (Jul., 1965), p. 409.
- William, L. M. (1998). False Alarms Buffet Pilots, Air Controllers, Los Angeles Times, April 1998. <http://articles.latimes.com/1998/apr/06/news/mn-36621>. Accessed November 2018.
- XSENS (2018). AHRS Attitude Heading Reference System: <https://www.xsens.com/tags/ahrs/>. Accessed September 2018.
- X-IO Technologies (2018). Open source AHRS with x-IMU: <http://x-io.co.uk/open-source-ahrs-with-x-imu/>. Accessed September 2018.